Department of Physics and Astronomy
University of Heidelberg

Bachelor Thesis in Physics
submitted by

Jan Philipp Beckmann

born in Bamberg (Germany)

2020

Observations and analysis of the high-z gravitationally lensed quasar APM 08279+5255

This Bachelor Thesis has been carried out by Jan Beckmann at the
Landessternwarte LSW of the Center for Astronomy ZAH in Heidelberg
under the supervision of
Prof. Dr. Jochen Heidt

Observations and analysis of the high-z gravitationally lensed quasar APM 08279+5255

Jan Philipp Beckmann

Abstract (Deutsch):
In dieser Arbeit wird ein neuer, hochaufgelöster AO-Datensatz des dreifach gelinsten Quasars APM 08279+5255, welcher mit dem LUCI-Instrument des Large Binocular Teleskops LBT im Nahinfraroten (J,H,Ks-Band) aufgenommen wurde präsentiert. Dieser wird mithilfe von Aperture- und PSF-Photometrie analysiert und modelliert. Ausserdem wurde eine mögliche 4. Komponente des Systems im Ks-Band gefunden und Detektionslimits berechnet sowie die Position einer zugehörigen Linsengalaxie eingeschränkt. Zusätzlich wurden LBT ESM Daten aus in den H,Ks-Bändern untersucht um Ergebnisse aus den vorherigen Beobachtungen zu bestätigen.

Abstract (English):
In this work we are presenting a new, high resolution NIR (J,H,Ks-Band) AO-dataset of the triple gravitationally lensed system APM 08279+5255 observed with the LUCI of the Large Binocular Telescope LBT. A detailed photometrical analysis of the object is carried out using both aperture and PSF-photometry techniques. Additionally we find a possible 4th component in the Ks-Band data and estimate detection limits for it's observation aswell as constraining the position of a corresponding galaxy. Furthermore LBT ESM H,Ks-Band NIR observations are analyzed to validate results from the discussed dataset.

Contents

Chapter 1

Introduction

1.1 Theoretical Foundation

1.1.1 Cosmological redshift

One of the most important terms in cosmology is the cosmological redshift z which is defined as:

$$z = \frac{\lambda_{obs} - \lambda_{em}}{\lambda_{em}}, \tag{1.1}$$

where λ_{obs} and λ_{em} are observed and emitted wavelengths of the source radiation, respectively [1]. This relation is also valid for the Doppler shift z, however, cosmological and Doppler redshifts have different nature. Doppler shift is caused solely by the relative velocity between the source and observer (e.g. by peculiar velocity of observed galaxy). The cosmological redshift is the result of expansion of the Universe: as the size of the whole Universe increases, so does the wavelength of emitted light [2].
On the other hand, the expansion of the Universe is characterized by the dimensionless scale factor a, its time evolution is a result of the Friedman-Equation, a derivation from the Einstein Field Equations under the assumption of a metric conform to homogeneity and isotropy of space. This equation relates the dynamics of space time (represented by H^2 and a) to its content today composed of radiation $\Omega_{R,0}$, matter $\Omega_{M,0}$, spatial curvature $\Omega_{k,0}$ and the Cosmological Constant $\Omega_{\Lambda,0}$ [1]

$$H^2 = H_0^2 \cdot \left[\Omega_{0,R} a^{-4} + \Omega_{0,M} a^{-3} + \Omega_{0,k} a^{-2} + \Omega_{0,\Lambda}\right] \tag{1.2}$$

Here $H = \frac{\dot{a}}{a}$ denotes the Hubble-Constant (that is in fact not a constant, since $a, \dot{a}$ are functions of time) which was first introduced by its eponym Edwin Hubble when observing relations of redshift ($\sim$ apparent recessive velocity v) and distance D to galaxies:

$$v = H_0 \cdot D \tag{1.3}$$

H_0 is the Hubble constant at "t = today". This relation is also described as the Hubble flow and one can conclude that if the separation between two objects which are subject to the Hubble Flow

is d_0 at the reference time t_0, the distance between them at some time t is given by:

$$d(t) = d_0 \cdot a(t) \tag{1.4}$$

The scaling applies to the wavelengths as well:

$$\lambda(t) = \lambda_0 \cdot a(t) \tag{1.5}$$

. Hence the equation 1.1 can be rewritten as:

$$1 + z = \frac{\lambda_{obs}}{\lambda_{em}} \qquad \text{with} \qquad \frac{1}{a} = 1 + z \tag{1.6}$$

Due to this stretching of wavelengths, the rest-frame spectra of distant galaxies and quasars with their characteristic features - for example, Lyman series - are oberved at lower energies or larger wavelengths. This is one reason why objects (with high Luminosities in the UV or optical) at large values of z are often observed in the Near-Infrared NIR.

1.1.2 Quasars

A quasar (or quasi-stellar object, QSO) is an extremely bright active galactic nucleus AGN with a supermassive black hole surrounded by an accretion disk.

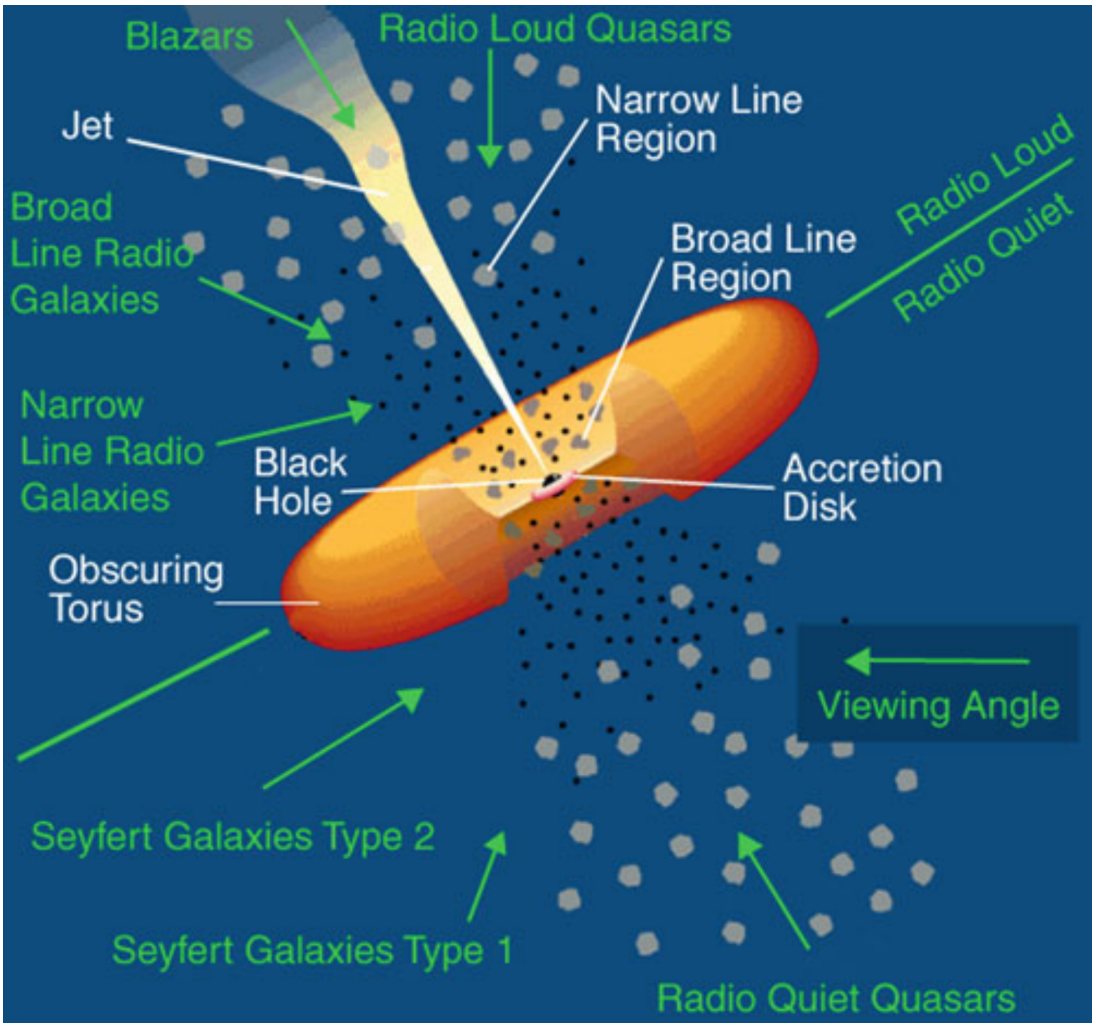

Figure 1.1: schematic illustration of an AGN, note that many different names exist due to the observational properties varying strongly by the viewing angle; at the time when these nomenclature were introduced it was not yet known that they have a common origin, figure from [1]

These objects can not be resolved optically but appear point-like, hence the name quasars. Quasars radiate in a wide wavelength range from X-ray to radio with the flux variation depending on the certain quasar and on wavelength. The optical spectrum of quasars is a very blue continuum with strong emission lines. The continuum spectrum of quasars consists of two major components, a thermal continuum in the UV and optical originating from the black hole accretion disk and a power

law spectrum for longer wavelengths (such as radio) with the spectral index α:

$$S_\nu \propto \nu^{-\alpha} \tag{1.7}$$

This spectrum is created by electrons following spiral paths in the magnetic fields of a relativistic jet, being constantly accelerated by the Lorentz force and thus emitting electromagnetic radiation. The optical and UV spectra of quasars feature very broad strong emission lines (sometimes also absorption lines) due to doppler broadening such as Balmer series, Lyα of hydrogen, and metal lines. These broad emission lines often have FWHM of $\sim$ 10000 km/s; "narrow" emission lines have FWHM of $\sim$ 100 km/s which is still much higher than characteristic velocities in normal galaxies [1]. All these different spectral components of a QSO (which can also show strong variation in short timescales, especially the emission lines) result in a very complex spectrum of this type of object:

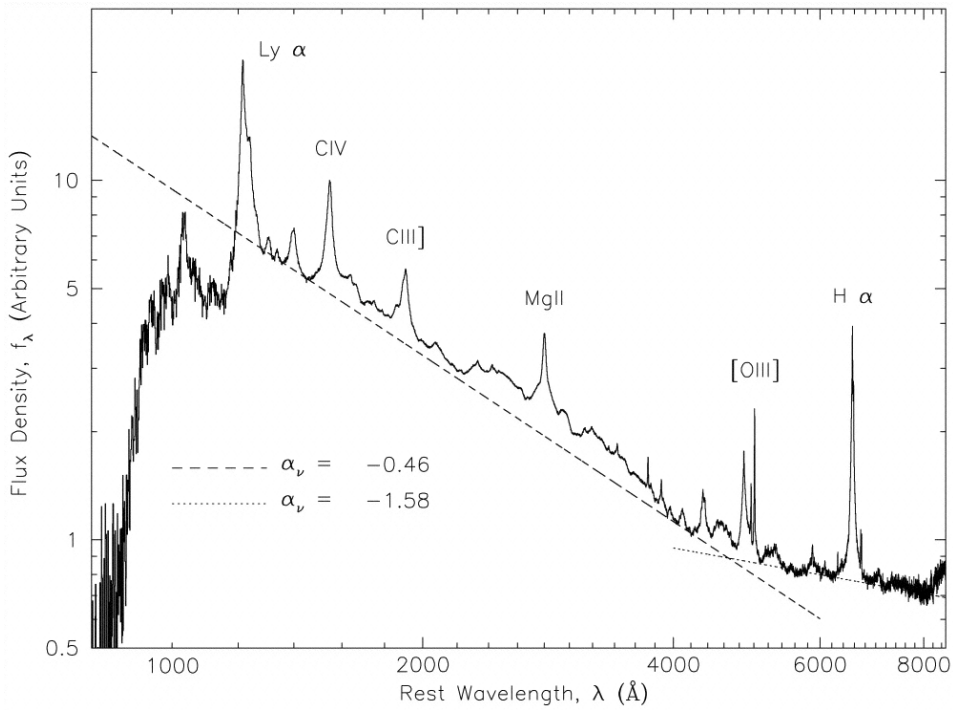

Figure 1.2: SDSS composite QSO spectrum from 2200 different objects, figure from [17]

When imaging (for e.g. a morphological analysis and photometrical data) one integrates the spectral energy density over the filter-bandpass in order to obtain the total flux in a given filter band. Considerable dust extinction in many QSO targets and a better strehl value of AO observations at higher wavelengths (see section 2.1 and 5.1) makes highly reshifted targets (like our subject of interest) well suited for observations in the NIR.

1.1.3 Gravitational lensing

Galaxies, clouds of gas, and dark matter can affect light from a quasar or any distant object along its way to the observer. As the light passes through the curved spacetime around the massive object, it follows the "shortest" (in other words: extremalising $ds^2 = g_{\mu,\nu}dx^\mu dx^\nu$) possible worldline, called a geodesic. This phenomenon is analogous to a normal refraction of light by a glass lens and may result in multiple images of the source. However, since the curvature of spacetime determines the refraction angle and not the refractive index of e.g. glass (that is strongly wavelength dependant), it is the same for every wavelength of light. For this reason there's no such effect as chromatic abberation resulting in the refracted images of a source having the same color (or more generally speaking: Spectral energy distribution) when neglecting effects of gravitational redshift.
The angular deviation of a photon passing at a distance r_0 from an object of mass M is given by [4]:

$$\phi = \frac{4GM}{r_0 c^2} \tag{1.8}$$

With the distance to the source d_S and distance to the lensing mass d_L it can be shown that the angle θ between the lens and the image of the source must satisfy the following equation (see fig. 1.3):

$$\theta^2 - \beta\theta - \frac{4GM}{c^2}\left(\frac{d_S - d_L}{d_S d_L}\right) = 0 \tag{1.9}$$

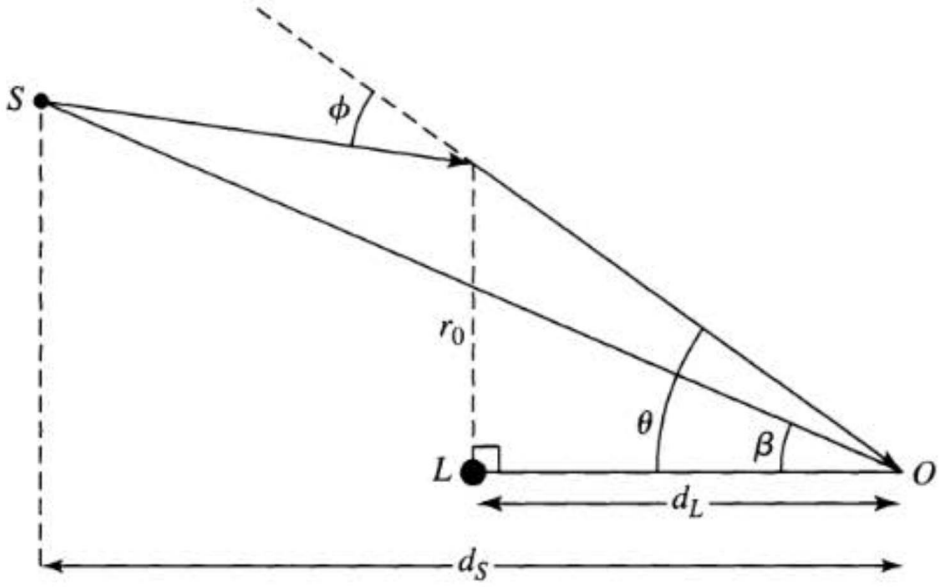

Figure 1.3: The geometry for a gravitational lens. Light from the source, S, passes within a distance of approximately r_0 of a lensing point mass on its way to an observer at O. All angles in the image are greatly exaggerated (from [4]).

This equation has two solutions θ_1 and θ_2 so that:

$$\beta = \theta_1 + \theta_2 \tag{1.10}$$

and

$$M = -\frac{\theta_1 \theta_2 c^2}{4G} \left(\frac{d_S d_L}{d_S - d_L} \right) \tag{1.11}$$

If a quasar or another bright source lies exactly along the line of sight to the lensing mass, an image of the form of Einstein ring around the lens emerges. The radius of this ring, θ_E, can be derived from the equation 1.9 with $\beta = 0$:

$$\theta_E = \sqrt{\frac{4GM}{c^2} \left(\frac{d_S - d_L}{d_S d_L} \right)} \tag{1.12}$$

It is a good estimation for the apparent angular scale of the phenomenon and relates and observational quantity to an intrinsic quantity of the system. So far, the lensing object was represented by a point mass to simplify the calculation. A much better model for a lensing galaxy is an isothermal ellipsoid around a central core. In this case, three or five images of the source are observed [4].

1.2 Previous Research

Discovery

The quasar APM 08279+5255 has been discovered and identified in 1998 by M. Irwin et al. [13]. A simple photometric and spectroscopic analysis of this object at low resolution has been done, determining a high redshift of z=3.87 and suggesting a very high intrinsic bolometric luminosity of $L_{bol} \sim 5 \cdot 10^{15} L_{\odot}$ making it the most luminous object known at that time. However, magnification effects from gravitational lensing are suggested [13].

First structural analysis

About 2 years later, a team of E. Egami et. al. [9] conducted NIR observations with the NIRC instrument of the KeckI-Observatory at significantly higher resolution than previous observations of this object. After PSF-modelling two gravitationally lensed components, another 3rd component has been found. Photometrical magnitudes and flux ratios of all 3 components distributed over 0.4" have been measured [9].

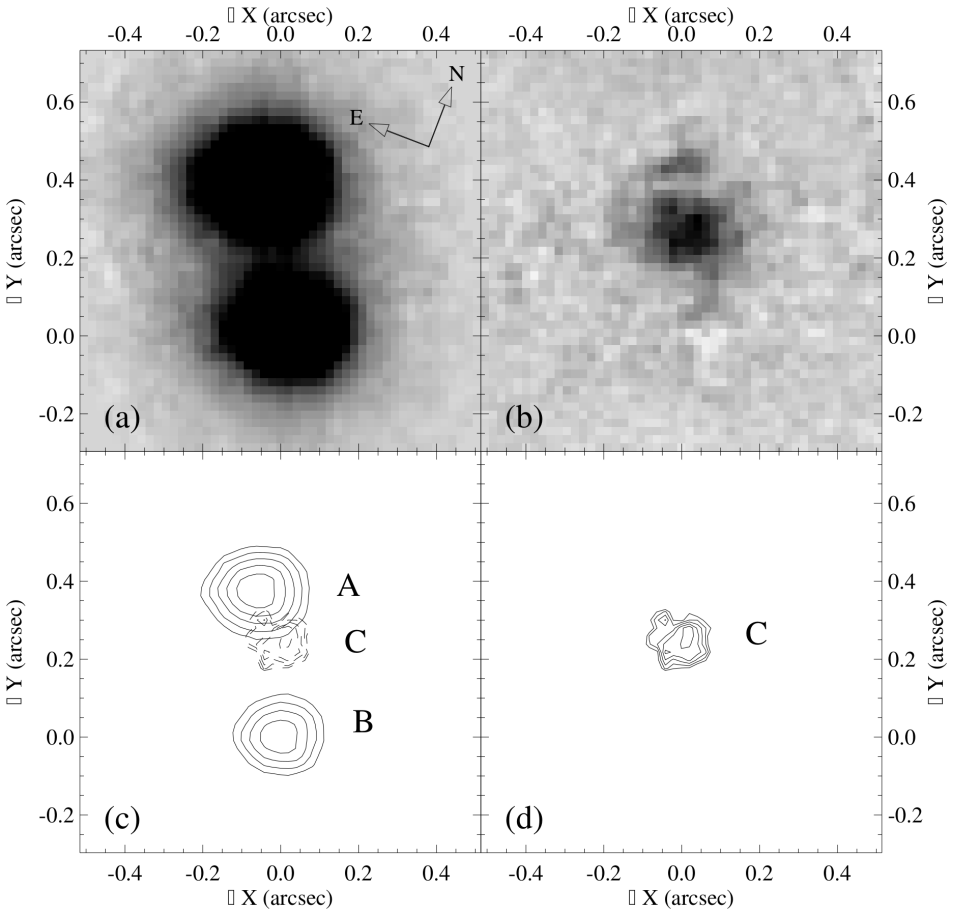

Figure 1.4: Structural analysis of the lensing system, discovery of a third component, graphic from [9]

Components	ΔX (arcsec)	ΔY (arcsec)	$\Delta\alpha$ (arcsec)	$\Delta\delta$ (arcsec)	Flux Ratio	K	χ^2/dof	FWHM (arcsec)
A.....	−0.060	0.377	−0.191	−0.330	1.28	12.82	0.93	0.15
B.....	0.000	0.000	0.000	0.000	1.00	13.09	0.93	0.15
C.....	−0.002	0.245	−0.090	0.228	0.26	14.55	0.92	0.15
Total.....						12.08		

Figure 1.5: Relative fluxes of the 3 discovered components in the K-Band, Table from [9]

Also, two lensing models, one with the assumption of the 3rd component being the lensing galaxy and one with 3 individual quasar images, have been investigated. A high magnification of up to 100 has been determined for the 2 component model, whereas a lower magnification of ∼10 can be achieved by the 3 component model [9]. The latter model is preferred by a number of observational reasons described in the paper, and suggests a massive elliptical galaxy as a lensing source at z ∼ 3. New observations in 2013 by S.Oya et. al. [19] with the Subaru Telescope using AO-imaging in the 3.05 μm, L' and M'-Bands at higher resolution, show the same structure and confirm the 3rd component to be a lensed image by color comparison. Furthermore a variation in total flux and flux ratios of the brightest components from the results of [9] has been observed, suggesting microlensing events occuring in the AGN. Also other observations claim to have detected a significant amount of molecular gas and star formation in the host galaxy [20]. Literature magnitudes obtained via simbad from the 2MASS [15] and SDSS [16] are:

r	z	J	H	K
14.864 ± 0.003	14.639 ± 0.005	13.410 ± 0.027	12.661 ± 0.026	12.050 ± 0.023

Table 1.1: Photometrical magnitudes from the 2MASS [15] and SDSS [16] catalogues

This table suggests that the object is graduately getting brighter for longer wavelengths. But this is not the case (see fig. 1.6 for the spectral energy distribution), because the magnitudesare defined with respect to a standart object (in the most popular cases Vega → VEGAMAG or the Sun → AB-mag) that has a spectral energy distribution declining more steeply at longer wavelengths than that of a QSO.

Spectroscopic Analysis

Parallel to the structural analysis of the system, numerous spectroscopic investigations of the object have been conducted. Subjects of study were the gas dynamics of the AGNs dust torus [21] as well as the variability of emission- and absorption lines [22]. The most recent UV and optical rest frame spectrum has been aquired by F.G. Saturni et. al. [7] with the TNG observatory:

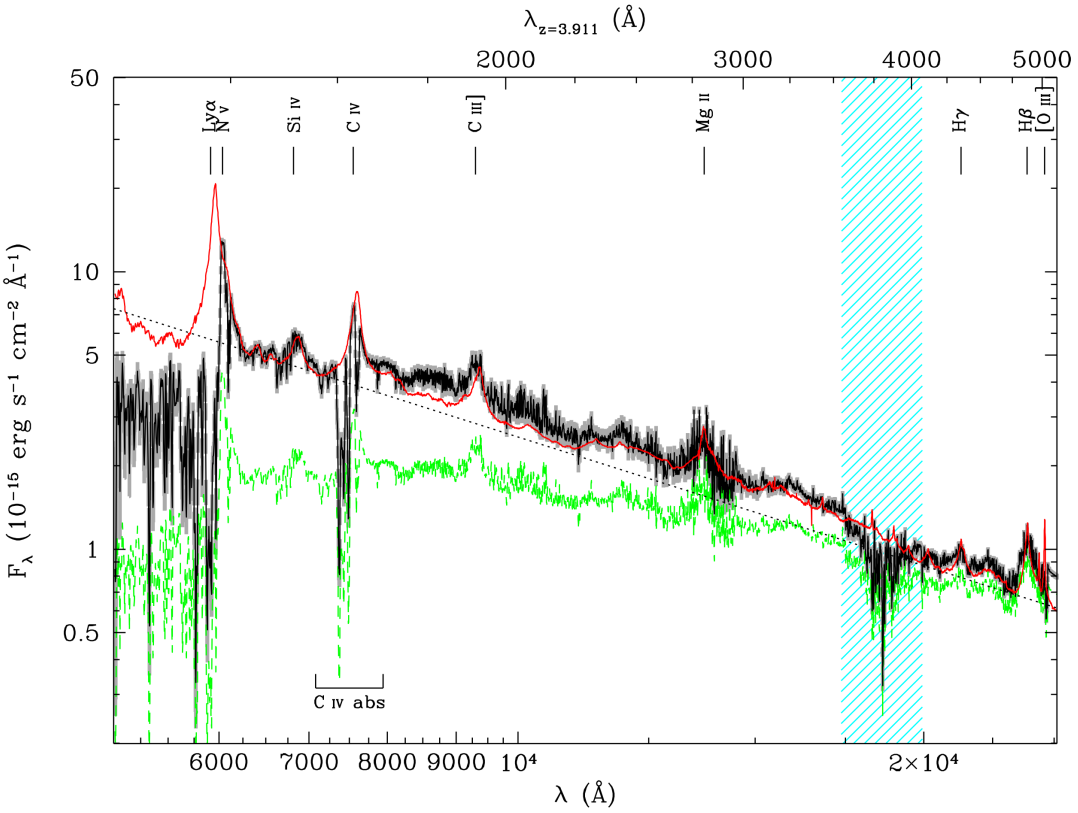

Figure 1.6: The UV-optical rest frame spectrum of APM 08279+5255, green plot shows the spectrum before dereddening, graphic from [7]

We can distinctevly see the broad absorption line BAL features of the object, as well as a significant impact of dust extinction over the course of the whole spectrum (note the difference between the green and black graph).

1.3 Objective of this work

Although there have been many observations of this fairly popular target, the nature of the whole gravitational lensing system is not entirely resolved. To this day no gravitational lensing source (most

likely a massive lensing galaxy) has been discovered. That would be needed to very predictions of previously conducted simulations. Also the structure of this 3 component lensing system is compared to other systems very odd, suggesting possible additional components. The imaging observations previously done on this target all have a comparably low SNR (only ~ 5 min with 8m aperture) for those at a high Adaptive Optics AO supported resolution. We therefore want to perform a more detailed analysis of the lensing system, with the objective of finding new components or a lensing galaxy, using the LBT's AO capabilities in high resolution and investing more integration time for better SNR data. This work is intended to be the foundation for modelling the gravitational lens system and will conduct the data reduction, photometrical study and basic morphological analysis of the aquired data set.

Chapter 2

Observations and Instrumentation

2.1 Object-based requirements

Since the main objective of the observations is a morphological and photometrical analysis of the target APM 08279+5255 we want to make sure to choose the right filters in order to detect as much signal as possible while still having the option to use a powerful adaptive optics (AO) system. We have already seen in CPT.1 that observing the quasar in the Ks-Band (that is less affected by sky background emission lines than the standard K-Band) out of all the Filters available at the Telescope might be the most beneficial (see Table 2 in [5] for detailed information on the different filters). As we are primarily interested in a detailed structural analysis of the object, we want to make sure to take the deepest dataset at a maximum possible resolution available in this Band. Also an AO-system like it is used in the LBT works best in a longer wavelength regime, since the Fried-parameter scales as follows:

$$r_0 \propto \lambda^{\frac{6}{5}} \tag{2.1}$$

This parameter is a measure of the scale of athmospheric distortion, a larger value is more favorable since a larger scale of the distortion also means less integrated variation along the line of sight and a higher threshold for seeing-limitation with a telescope of given aperture. There are less strong corrections to be made by the Adaptive Optics giving in general a better result in achieved resolution and strehl ratio in the Ks-Band. The strehl ratio is a dimensionless parameter

$$SR = \frac{I(0)}{P(0)} \tag{2.2}$$

that relates the maximum intensity of the observed point spread function PSF to its theoretically achievable value and is a good measurement for the quality of an optical system, especially when working with AO. The LBT is capable of achieving an AO strehl ratio of up to 80% in the Ks-Band, which is amongst the highest values for any AO-system [24]. Also, effects of dust absorption e.g. because of a galaxy along the line of sight (maybe the lensing galaxy?) or in the neighborhood of the quasars power source itself (e.g. dust torus) are lowest at higher wavelength. This is an important point that has to be taken into consideration, since APM 08279+5255 is classified as a BAL

(broad-absorption-line) -quasar, showing as the name might suggest, irregularily strong and broad absorption in the UV-part of the spectrum [1] [9] [7].
For an object at a redshift of z = 4, the central wavelength λ_c of the Ks-Band of 2.163 μm (see [5]) corresponds to 432.6 nm in the objects restframe, whereas the λ_c of the J- and H-Band corresponds to 249.4 nm respectively 330.6 nm. One might argue that in order to avoid dust extinction, you want to observe at significantly higher wavelength in the objects rest frame (in the I-Band or redder), but at a redshift of z 4 this lies outside of the working range of any instrument used at the LBT observatory and might also be subject to general observational constraints. Nevertheless, due to the inverse wavelength dependancy $\propto \lambda^{-1}$ (assuming $\lambda \approx d$) of dust extinction and broad-absorption-line features of this object, this will give an advantage compared to observing in even bluer wavelength.
Nevertheless there are a couple of observational challenges to overcome when observing with the AO in the Near-Infrared regime. As we already talked about absorption, it is also necessairy to mention that not only the observed object or interstellar show this effect, but also the athmosphere is (in comparison to the optical) a major contributor in the NIR (telluric absorption). There are multiple absorption bands in the NIR due to vibro-rotational excitation of molecules like CO, CO_2 and H_2O that constrain the observable wavelength bands. The NIR-filter system is oriented by those telluric absorption lines.
But not only athmospheric absorption causes observational limitations, the effect of athmospheric emission is present aswell and poses a number of problems. The overall sky-background flux is significantly higher in the NIR than in the optical. For comparison, in the V-Band the sky brightness at the La Silla observatory (far away from any artificial light sources) during a moonless night is about 21.9 $mag/arcsec^2$, while beeing 13.0 $mag/arcsec^2$ in the K-Band under the same conditions. It consists of numerous emission lines (at very high altidudes > 85km) and thermal radiation, and can be variable (up to 10%) on very short timescales (minutes) [6]. Especially the emission component is highly variable, producing together with temperature changes, the strongest variability in the J,H-Bands in the first/last 2hrs of the night [6].
A bright and variable sky-background limits the maximum exposure time of a single exposure (especially in the K,Ks-Bands) and favors shorter individual exposure times. It is desirable to reach background limitation, but not to expose unnecessairily longer since the SNR gain is generally lower in this regime compared to the read-out noise regime. The objects coordinates (J2000) are RA = 08h 31m 42s and DEC = $+52°45'18''$, hence the best time in the year for observing is from November to March. In this period the object is high above the horizon during the middle of the night, minimizing both seeing effects and sky-background (+ its variability).

2.2 Instrumentation

2.2.1 The Observatory

Figure 2.1: The Large Binocular Telescope LBT [8]

The Large Binocular Telescope Observatory (LBTO) is located on the Emerald Peak Mountain in the Pinaleno Mountains in southeastern Arizona at an altitude of 3200m. This area is part of the Coronado National Forest. The LBTO headquartes are on the Tucson campus of the University of Arizona. It is an international collaboration between the University of Arizona, the Italian National Institue of Astrophysics INAF, the German LBTB and a number of other US universities [8]. The LBT consists of two identical 8.4m telescopes mounted side-by-side on a common Alt-Az-mount with a effective colletive area of a single 11.4m telescope. Its mission is both to offer two individual state-of-the-art 8m-class telescopes and to be a pioneer in developing and testing new technologies such as NIR-interferometry with the 22.8m baseline between the two primary mirrors for the new ELT generation of telescopes.

2.2.2 The Instrument

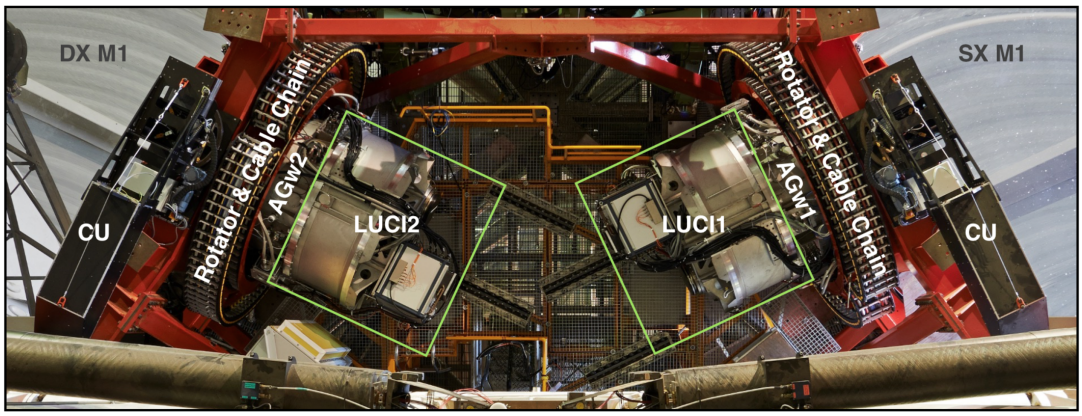

Figure 2.2: The LUCI instruments mounted at the gregorian f/15 focus [5]

For our observations there best suited instrument is the LBT Utility Camera in the Infrared (LUCI) . There are in fact two identical LUCI instruments (LUCI1 and LUCI2), that are mounted in the f/15 Gregorian focuesses of the 2 seperate telescopes (see fig below). The instrument was comissioned by the LBTB with lead construction and design by the Landessternwarte Heidelberg. Each LUCI instrument is a cryogenic multi-mode NIR instrument with a wide range of capabilities such as imaging, longslit and MOS spectroscopy over a 4x4-arcminute field of view in a seeing limit mode. But theres also an option of performing high resultion imaging or longslit spectroscopy over an 30x30-arcsec FOV with the help of a powerful adaptive-optics system [5]. 672 actuators located under the thin and highly flexible secondary mirror correct athmospheric distortions of the wavefront measured with a natural guide star at a rate of up to 2000 Hz. Under optimal conditions, this can yield a resolution down to a FWHM of 64 mas [24].
These specifications make the LUCI instruments a perfect choice for observing a highly redshifted multi-image gravitational lensed quasar such as our object of interest. This high spatial resultion is the key requirement of splitting the previously detected components into more possible components, or detecting the source of the lensing potential (such as a lensing galaxy) near bright lensed images. Both instruments work in a wavelength range in the Near-Infrared of about 0.95 μm up to 2.4 μm at the red end of the K-Band. As for reasons mentioned in section 2.1, observing in the Near-Infrared, more specifically the J,H,Ks-Bands that are available at the LUCI instruments, will also give us the opportunity of achieving a higher SNR for our object than in the e.g. optical if challenges like the bright sky background are managed correctly. Each LUCI instrument features a modern Hawaii 2-RG detector that can be equipped with 3 interchangable cameras (N1.8, N3.75, N30) producing different image scales as required for different scientific applications.
Producing a pixel-scale of 15 mas, the N30 camera is designed for the use of adaptive-optics in imaging at the telescopes diffraction limit and hence the choice for our observations. We will also

use imaging data taken with the N3.75 camera at a later point of the work. This camera is featuring the Enhanced-Seeing-Mode ESM, which corrects tip-tilt and low order zernike modes at a frequency of up to 100 Hz. This offers an increased resolution at the benefit of using a 4x4-arcsec FOV and a pixel-scale of 12 arcsec/pix. We will discuss the objective and reasoning behind using observations of the Quasar in this configuration in CPT. 6. We will also further discuss the properties of Near-Infrared detectors such as the Hawaii 2-RG detectors used in the LUCI1 and 2 instruments in 3.1. This will however better fit into context in the section of data reduction, since those properties will directly infer which strategy has to be followed.

2.3 Data aquisition run

The observations of our target APM 08279+5255 in the J,H, and Ks-Band have been executed during the 2017/2018 winter run of the german LBTB contribution. Lead observer was J. Heidt supported by O.Kuhn, D.Huerta and G.Taylor. The Ks-Band data set was taken in the night from 29th December to 30th December 2017, using the LUCI2 instrument and the N30 Camera in full-AO mode. This night stood out with exeptionally good conditions for an AO-run. The seeing was reported of beeing between 0.7 and 0.5 arcsec thoughout the whole night at a very low humidity of 7% at the time of sunset.
However some transient issues of the star moving for a very small distances on the sensor after a dithering step producing double star shaped features, occurred later in the night after the observation of our target. The observations of APM 08279+5255 started at 6:32 UTC universal time with the AO correcting 36 zernike modes at a rate of 200Hz. They ended at 9:53 UTC only reporting a minor incident of opening the loop for one of the images in the series. In this time 118 frames of 60 sec each were taken for a total exposure time of 118 mins in the Ks-Band. This data set should outmatch the SNR of previous observations on this object using a full-AO system by a large margin unlocking the possibilities of a much more in depth study and discovery of new previously undetected components or a lensing galaxy.
However also two other data sets in the J- and H-Band were also taken in the following night from 30th December to 31st December. Those observations started at 6:59 UTC until 10:29 UTC and collected 59 frames of 60 sec each for both J- and H-Band. However the seeing was reported to be higher than in the previous nights at 0.8-1.2 by DIMM and the observning logs mentioned that thin cirrus clouds started to move in just before the start of observation. Unfortunately the recovered DIMM data from this night, does not include measurements of the sky background or transparency, with which we would be able to quantify the influence of the cirrus clouds.
Altogether the observations in the Ks-Band with their higher total integrated exposure time, also being intrinsically less seeing compromised, are intended to the structral analysis of the object, while the J- and H-Band observations are more suited as a verification of the results by checking the color of different components. We hence do not require the same SNR or resolution as in the Ks-Band.

Chapter 3

Data reduction

3.1 Technical background and data reduction principals in the NIR

Unlike in the optical, for observations in the NIR regime specialised detectors are used instead of CCDs. Those detectors (like the Hawaii-2RG detectors of LUCI) are called Hybritized HgCdTe arrays.

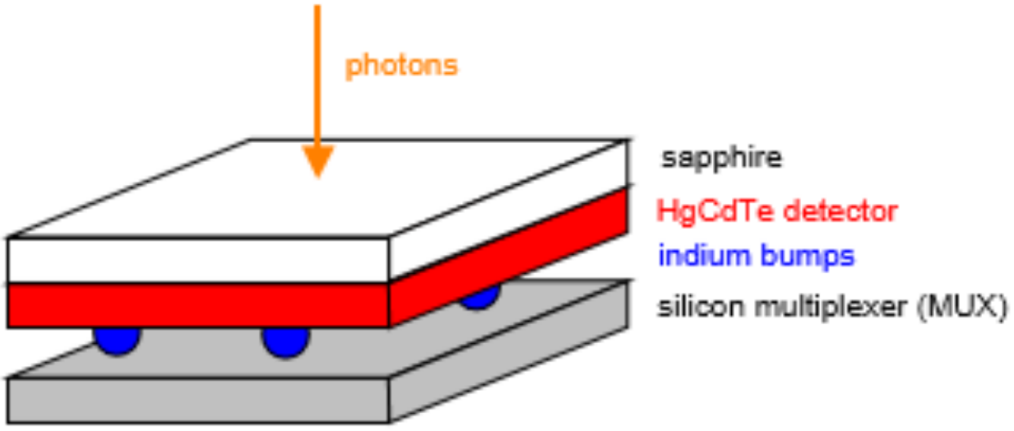

Figure 3.1: schematic structure of a Hybritized HgCdTe NIR detector, graphic from [6]

They can operate with a lower bandgap (between valence and conduction band) of their semiconductors in order to achieve a high sensititvity in detecting lower energy photons (such as in the NIR compared to the optical). Another advantage is that the photodetection and read-out process are seperated, allowing a non-destructive read-out. In order to reduce the effects of thermal noise inherent to a semiconductor based detector with a low bandgap, the system is operated at temperatures $\sim$

70K. When the detector is reset, a constant voltage is applied. Incoming photons deliberate charge and reduce the voltage to the point that saturation occurs when any residual voltage is depleted, hence no shutter is needed nor is a bias applied [6]. Due to the non-destructive nature of the read-out, multiple read-out techniques can be used optimise the read-out-noise and dynamic range of the detector. In our case there are 3 modes available [6] [5]

1. **Double Correlated Sampling DCR:** This method reads out the detector immedately after reset and at the end of integration

2. **Multiple Endpoint Read MER:** Also called Fowler sampling, this method uses multiple read-outs at the beginning and end of the integration reducing the read-out noise by a factor of $\sqrt{N}$ for N iterations

3. **Sample up the ramp SRR:** In this method, the pixel voltage is sampled multiple times during the integration. The Signal can be the result of a linear fit through the datapoints for each pixel or the difference of individual read-outs (for some special applications such as speckle interferometry). Information on saturated sources can be recovered.

For further details and the advantages/disadvantages of these modes, see the LUCI user manual [5]. In general, there are three different types of observational "errors" to be corrected for this type of detector. An additive error consisting of dark current and sky background and a multiplicative error, the inhomogeneous pixel illumination and sensitivity. Further errors are "cosmetical" errors such as malfunctioning pixels (bad-pixels) and crosstalk. Therefore there are three main steps in data reduction, correcting each of the different types of errors described in the follwing sections.
We are now going to discuss this procedure in detail for the Ks-Band series. For the J- and H-Band, the whole process has to be repeated seperately.

3.2 Background substraction

As it was already discussed in CPT.2, we know that the sky-background is a major problem when in NIR imaging. However theres are methods to take care of this issue in data-reduction. Together with the faily insignificant dark current (thermal signal) this is the major additive error to be corrected. The key strategy is to construct a model of the background, that respresents its intensity, spatial and temporal distribution as precisely as possible. This model can then be substracted from the image frames in order to remove the background flux and isolate the objects flux in the data before doing further steps in data-reduction.

Analysing the background of raw frames

To first get a glimpse on how our frames are affected by the sky-background, we want a rough estimate on its intensity, spatial and temporal distribution. A fairly simple method is to calculate the statistics of individual images or regions in these images for every frame in the data-set.

This can be done with the IRAF IMSTAT command, that also is able to output the statistical measurements as a table ready to use for any further data analysis. Theres also a possibiliy of applying an outlier rejection in calculating the statistics (*kappa-sigma-clipping* and range selection *lthreshold/hthreshold*). We have not yet applied any form of data-reduction, nor removed any artefacts, consequently this is a good way in helping to making the estimates more robust.
Note that the calculation of the mode (the most frequent value in a set of values) is the most meaningful in the statistical analysis at this point. We expect the histogram to show a distribution of two major features: a gaussian peak for the background and a non-uniform distribution for the object skewing the total distribution to higher values than the background. Since distinguishing statistically between object and backgound is very difficult at this stage of the data-reduction, we need to use a statistical measurement that represents the mean background intensity fairly well. Just calculating the mean or median of this complete skewed distribution will not do this. Due to the object occupying only a small fraction of pixels in the frame, the background distribution has in general higher values than that of the objects. Consequently, calculating the mode of the total distribution will give us a more robust measurement of the mean background intensity. Unfortunately errors have been made at the time of data reduction always using the median when calculating the background, that couldn't be corrected anymore at the time of writing the thesis, since the whole data reduction procedure would have had to be repeated.

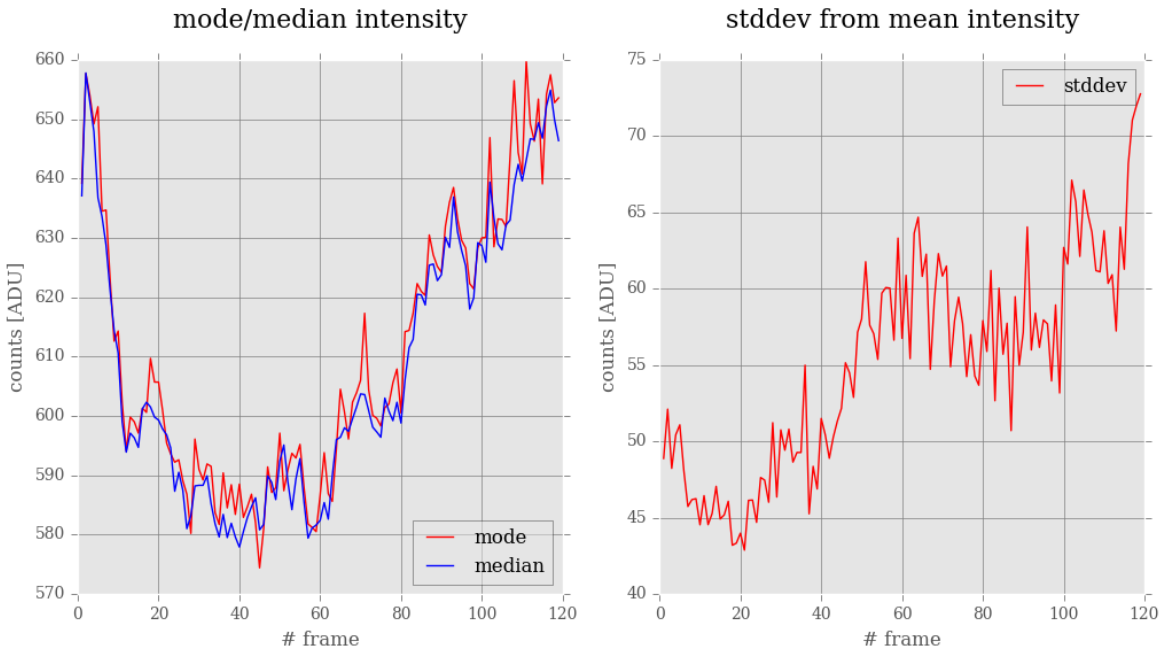

Figure 3.2: Image statistics of raw frames

However most of the time (especially when the object does not cover a large area of the FOV) both measurements do not differ by a large margin. The results for the statistics of the whole frame for every frame in the series are shown in figure 3.2.

4 Strategies of Background Substraction

Irrespective of the results from the estimates before, there are 4 common strategies of different complexity to apply for background substraction. Each strategy assumes a different degree of background variation, on which basis models are created. We will quickly explain the different approaches, their implementation and results for each strategy and furthermore argue which method is the most suited for our data-set.

Strategy 1: Static simple median substraction

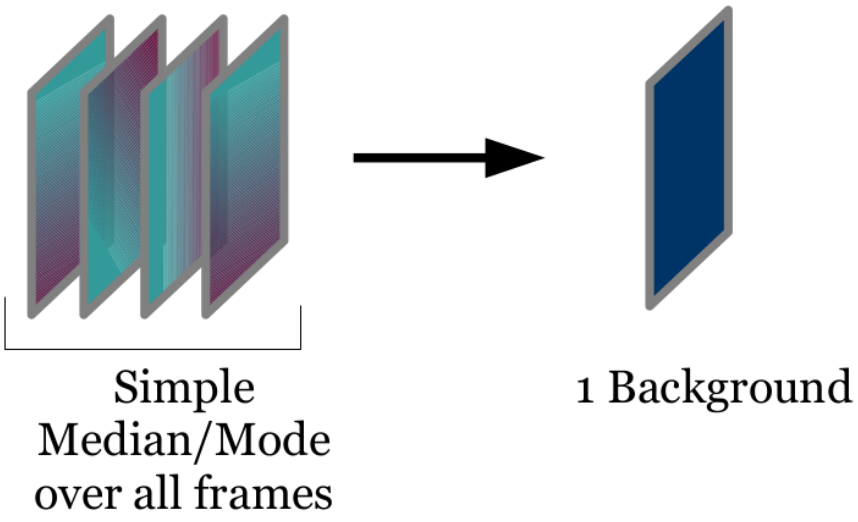

Figure 3.3: Strategy 1 background model illustration

This strategy assumes neither temporal nor spatial background variation, hence a static homogeneous background throughout the whole series of frames. As one might expect, this method is not expected to work well and more or less serves as a reference on how much better more realistic assumptions are. However in order to perform this method, the median is calculated using the IRAF IMSTAT command for every image, then the median is calculated from the individual results and afterwards and substracted via IRAF IMARITH from the subframes.

Strategy 2: Time variating simple median substraction

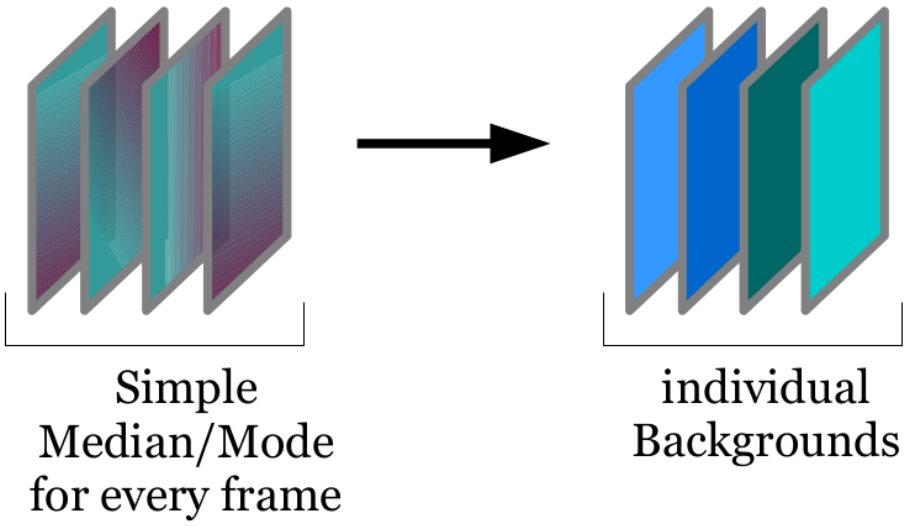

Figure 3.4: Strategy 2 background model illustration

Very similar to Strategy 1 we assume a spatially constant background in the individual frames (only one value is enough to describe the distribution), but this time allowing changes in time along the series of frames. Thus we substract the mode of each frame from each individual frame with the IRAF IMARITH command. It will give us a simple model on how the background changes with time. Furthermore in order to make the statistics more robust, we apply a mask to the frames before calculating. This is done with IRAF MKOBJECTS and uses the quasars coordinates from section 3.4 creating a box with value 0 (and value 1 elsewhere) that is multiplicated with the original frames.

Strategy 3: Skyframe background substraction

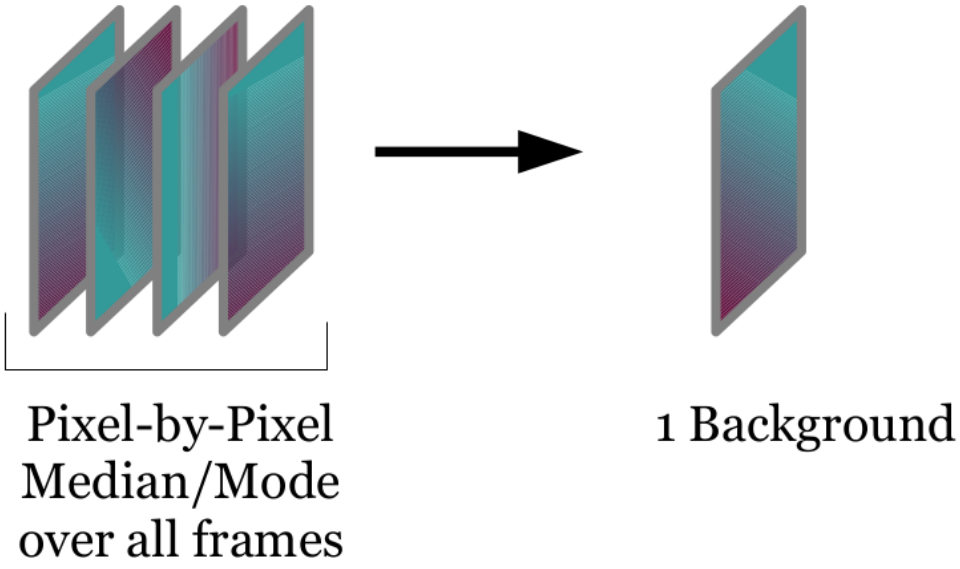

Figure 3.5: Strategy 3 background model illustration

Now we are going to drop the assumption, that theres no spatial variation in the frames FOV, but are going to remain assuming that the inhomogeneity is not changing with time but in total with a simple factor between every frame. To recover the inhomogeneity over the FOV we make use of the fact that we dithered every image and now can combine them using a strict rejection clipping away the object and just leaving an average of the background. Combination is done with IRAF IMCOMBINE, also using the option *scale = mode* and generaing a so-called skyframe as a result. This skyframe is rescaled with the individual frames mode for every frame in order to fit its overall background brightness and then substracted with IRAF IMARITH.

Strategy 4: Dynamical skyframe background substraction

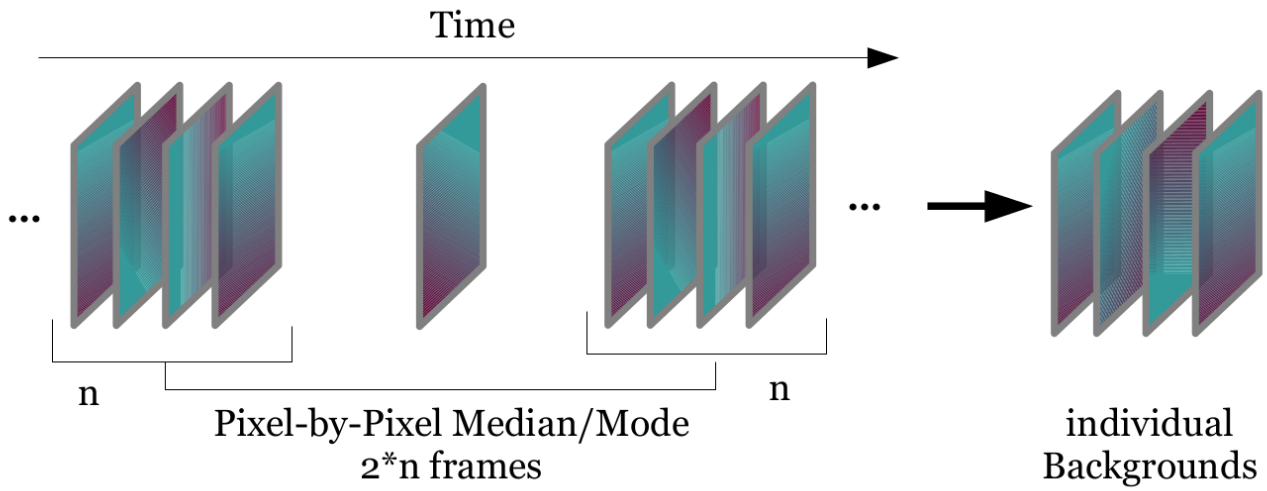

Figure 3.6: Strategy 4 background model illustration

This is the most complicated method based on the assumption of a both spatially and temporally variable background. It creates a background model for every individual frame by combining a number of dithered frames taken before and after the it. When determining the number of frames to combine into a background model we have to consider a tradeoff between the temporal resolution of the correction and the SNR of the background model to substract. Combining more frames taken before and after the frame to be corrected can be imagined as a convolution of the backgrounds time variation in our model. But using a very small number of frames for our background model leads to a very bad SNR of the model, that will degrade the SNR in our background corrected frame by at worst a factor of $\sqrt{2}$ if only one frame is used. As we are again using the frames containing the object for creating the model, it is advisable to mask it similar to the method described before in order to help the rejection algorithm with rejecting high intensities.

Evaluating the results of background substraction

Similarily to before we are examining the background with the image statistics. Therefore we are again using IRAF IMSTAT and plotting those measurements for the complete series of frames (figure 3.7):

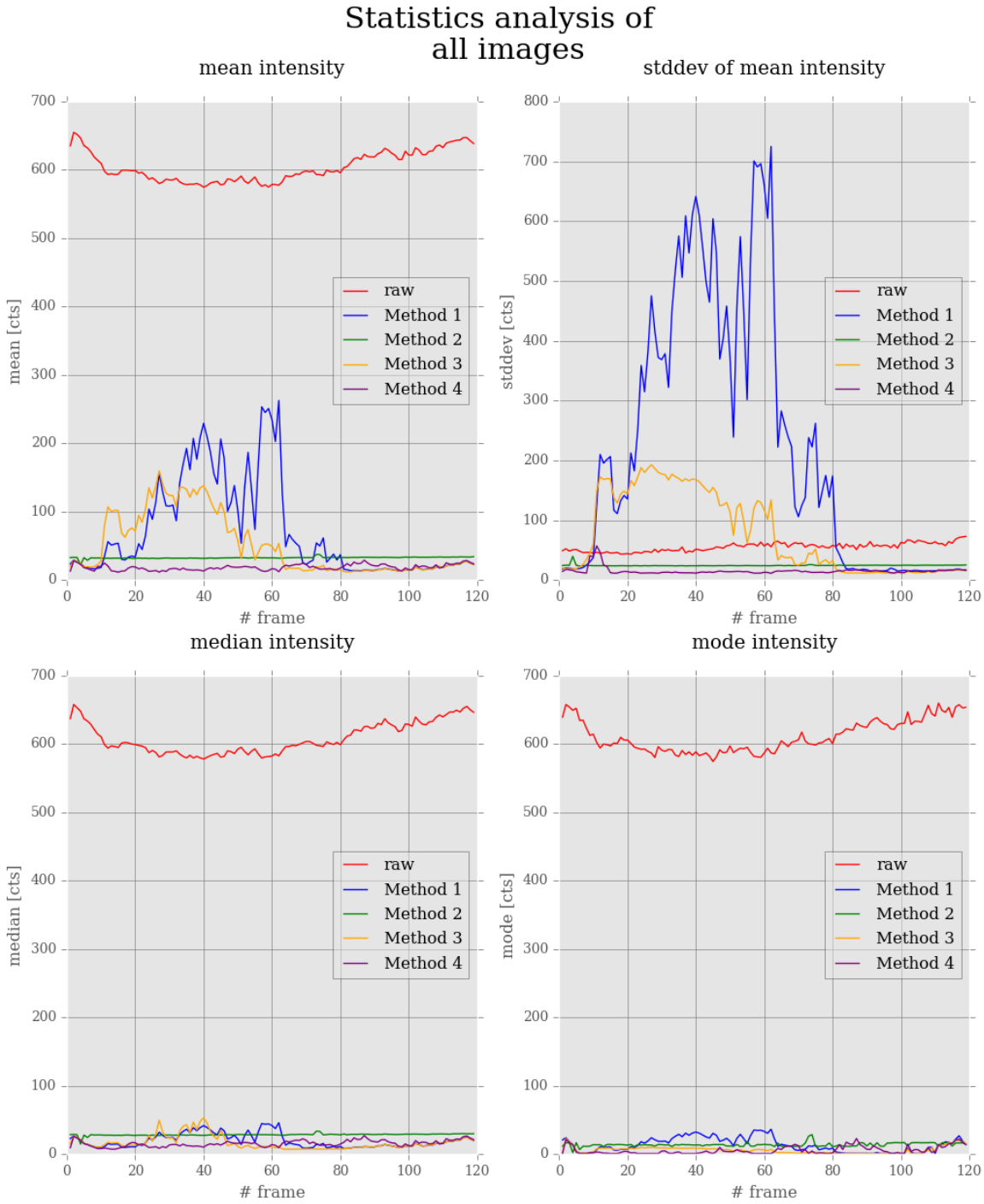

Figure 3.7: Strategy 4 background model illustration

In order to evaluate the results, we have to remember that it is most desireable to obtain a low median/mode intensity meaning that background substraction did a good job in modelling any variations in the integrated (per frame) background intensity over the course of the series. Also it is important to obtain the lowest stddev per frame as possible, since this is a measure of the background noise in the image as well as residual spatial variations in the individual images.
When examining the mean/median/mode plots for Method 2, one has to remind a inheritant artefact of the determination of the statistical values after their respective background modelling. In this method we calculated the background model as a frame with the median of the frame to be corrected as a value for every single pixel. If we substract this frame, the resulting median will just be lowered by the estimated median. This results in the medians of the corrected series always having the same value thoughout the series, with the exception to a couple of outliers due to the changing rejection constraints after substracting the median. We see that Method 4 yields a mode intensity closest to 0 over the series, as well as the lowest stddev (meaning least variations and noise in the background of the corrected images). Therefore we conclude that the dynamical Background substraction works best as expected, because it uses the most realistic assumptions. We are consequently using the results obtained with Strategy 4 for further data-reduction and data-analysis.

3.3 Flatfield correction

The necessity of using flatfields in data reduction

When analysing scientific data we always want to make sure that it does have the least, or at best no instrumental artefacts. Every detector based on pixel matrices such as e.g. CCD-Cameras or the Hybridized HgCdTe arrays used in the LBTs LUCI 1 and 2 instruments, suffers from a construction-related problem. The quantum efficiency (QE) of pixels is not uniform, it differs for every pixel and can also show larger scale structures caused by sensor defects and electronic deviced of the sensor or in its vicinity. These artefacts can be seen well in the flatfield example (fig.3.8) below.

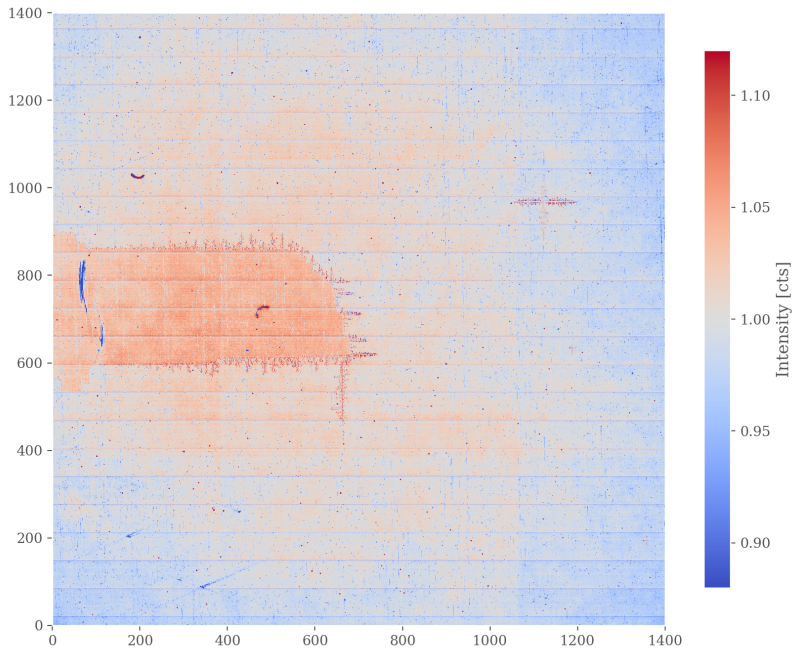

Figure 3.8: Example of a normalized master flatfield in the Ks-Filter

Furthermore every optical system, mainly image field corrector lenses and photometrical filters, leaves an artificial imprint in the fields illumination. These effects are commonly known as vignetting and are also to be corrected by the flatfield. Furthermore dust motes on the filters or any other optical element in the imaging train can also contribute to large scale artefacts. A proper flatfield is an accurate sensor map of the pixel-to-pixel inhomogeneities in quantum efficiency (QE), with has to be removed of all other instrumental effects (dark signal, linearity, illumination gradients, internal scattered light, etc.).

Observing and Creating Flatfields

Taking a flatfield requires a perfect homoheneous or flat (hence the name of these frames) light distribution to enter the telescope in order to isolate imprints of the instrumentation. To achieve this as best as possible, astronomers use different methods or homogeneous light sources.
In the data reduction for our data we use Twilight Flats, which take advantage of the sky beeing a spatially very homogeneous light source during twilight and better representin the spectral energy distribution of the sky-background at night (this is important because the QE of every pixel is wavelength dependent!).
To reduce the effect of photon shot noise, a series of 20 images is at high illumination well in the linear regime of the sensor is ($\sim$ 10k counts) taken and combined via median-kappa-sigma combination. Since the total sky intensity during twilight is highly variable with time, the individual frames have to

be rescaled with their mode first. This can be done either by estimating the mode with IRAF IMSTAT seperately and rescaling the images by hand with IRAF IMARITH or just using the parameter *scale = mode* (not median, since we always have a strongly skewed histogram!) in the IRAF IMCOMBINE command while combining the frames.
The same recipe is used to create another flatfield from a second series at low illumination (∼80 counts) with the same exposure time like the high illumination flats. Substracting the combined image from the one at high illumination corrects for any additive offsets and read-our or dark current patterns. In order not to distort the acutal fluxes in the data, the flatfield has to be normalized to a median of 1 using IRAF IMSTAT to estimate the median and IRAF IMARITH to divide by its value.

Applying the flatfield correction

Since all the imprints a flatfield is meant to correct for affect our scientific data are of multiplicative nature we will need to divide it by the flatfield pixelwise. The IRAF IMARITH command operating on a list of all individual scientific frames takes care of that.

Cosmetic Correction

After the flatfield correction we need one last step in data reduction before being able to stack the images and create our master frame. Every detector has a number of individual defective pixels (for our detector up to 0.5% !), either giving a significantly too high signal (hot-pixels) or no signal at all (cold-pixels). They show in every image and therefore have to be corrected before image integration. Doing it at this stage of the workflow is sufficient. These so-called Bad-Pixels are corrected by Bad-Pixel-Masks BPMs, that are created by filtering all pixels higher or lower than a certain sigma of the image's median. We have already prepared BPMs for both LUCI1 and 2 detectors at hand and only need to apply the correction with the IRAF command FIXPIX. Using default parameters, the correction replaces every bad-pixel with the median of its nearest neighbors.

3.4 Image integration

Calculating image shifts

Since our data is dithered, we need to shift every frame in order to be aligned with each other when executing the image integration. The LBTs Alt-Az mount uses very accurate autoguiding and a field rotator in order to account for any field rotation inheritant from this type of mount. We furthermore ignore field curvature [5] and therefore assume that a simple shift that can be calculated by comparing the coordinates of a single point in the field of view FOV is sufficient in order to align the frames well over the whole FOV. One could argue that we could just invert the dithering shifts used in the observations. However these were not available at the time of data reduction such that they have be calculated from the individual frames.
For this we use the IRAF Apphot CENTER command that will output the coordinates of the brightest

peak in a predefined box. The coordinates of the centerbox and its size has to be set such that our point source to align the images is well inside the box in order not to confuse it with other point sources. However in our case theres only one very bright object in the FOV, the quasar itself. But we have to take care since the quasar is composed of two very bright components with similar peak intensity. Tests showed that the algorithm manages the situation well and did always output the coordinates of the brighter component.
Having calculated the positions of the brightest quasar component in every frame we can use the first frame of the series (that also has the quasar located near the center of the FOV) as a reference frame and substract the coordinates from those of every other image. Further multiplying all coordinates by -1 will give the image shifts required for image integration. We save them in a text file for use in the IRAF IMCOMBINE command.

Checking the dithering pattern

In order to efficiently remove fixed pattern artefacts in the image integration process, it is important that a random dithering pattern (essentially not being a pattern) is used. Otherwise artefacts will be translated into the stacked image. Thus we are quickly reviewing the dithering pattern using the shifts calculated for successful image integration, which are essentially the inverted dithering steps.

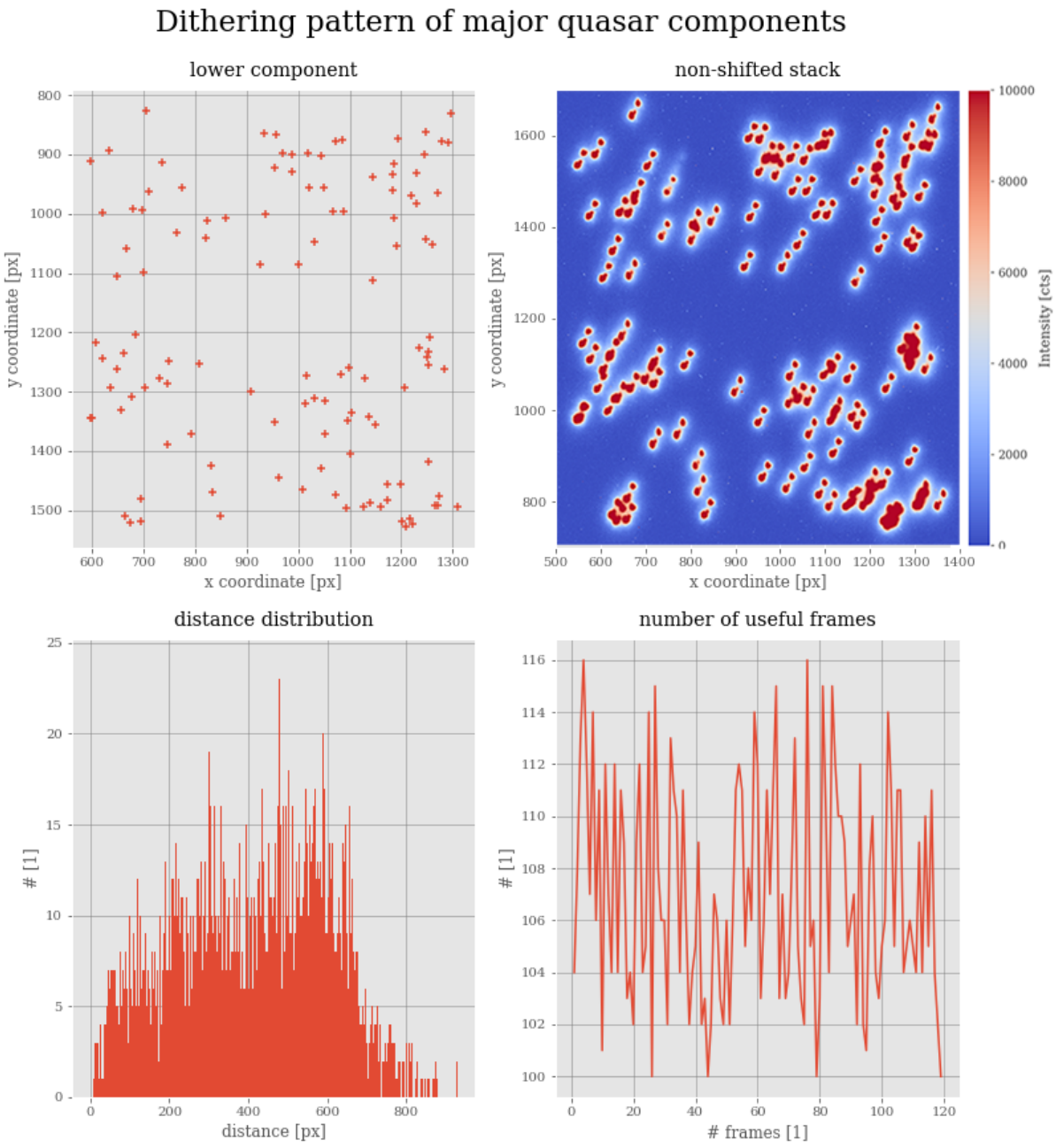

Figure 3.9: Dithering pattern of the Ks-Band series

Best results are achived if the object is placed on a different position of the sensor in every individual frame with the least possible overlap, or in other words the most distance from each other. The dithering pattern will also show if we integrate the frames without any shifts as the position of the

objects. The subplot about useful frames shows that our method of combining raw frames into skyframes is applicable, hence the dithering distance is large enough for always being able to "clip away" the object and obtain a background model. The number of suitable frames counts the number of frames in which the distance of the object to itself in other frames is larger than the assumed extend of the object.

Image integration (stacking) and estimating best rejection parameters

Image integration is a procedure used to combine inidivdual subframes of the same shorter exposure time into a single frame with the same SNR as a single exposure of the sum of all exposure times, if we assume the detector has no read-out noise and the frames are not dithered. This is certainly not the case, the used hybritized HgCdTe detector has a RMS read-out noise of about 5 ADU, but mainly due to the limited dynamic range, background variability (and a number of various other reasons) splitting into short exposures is necessairy. To combine our set of exposures we are averaging all frames (pixel by pixel).
Ideally the signal is the same in each subframe and therefore should not change at all during this operation while the noise declines by a factor of $\frac{1}{\sqrt{N}}$ where N is the number of subframes combined. Although we already took care of different types of technical artefacts in our data by previous steps of data reduction, there are still artefacts such as cosmics, walking pattern noise or sensor persistence, that have to be taken care of.
Now we see the necessity of dithering our images, since placing the object and the sky background at a different position of the sensor for every frame, artefacts will only occur rarely at a given pixel of the aligned image stack and can therefore be efficiently removed with an outlier rejection algorithm. Also cosmics that should only occur in one image at a given position will also be rejected by that algorithm.
As those artefacts also should occur less often at this point, we can use the operation average instead of median to combine our images and the *kappa-sigma-clipping* algorithm for outlier rejection. Additionally we can reject a number of high and low values of every pixel if the previous rejection is not efficient enough. One artefact, that is not going to be corrected is channel crosstalk, a common problem with Hybritized HgCdTe Detectors. More advanced methods are needed to remove this artefact, since in our case no data of an object of interest is compromised we wont attempt to remove it.
Even after a successful background substraction, the intensity of the background and/or object can still vary between different frames to combine. We therefore want to rescale our images by the mode (rember flatfield-correction, skewed histogram, gaussian noise + object), this is done with *scale = mode*. The whole image integration operation will be executed with the IRAF IMCOMBINE command. After a couple of iterations with different parameter settings, we find that the following work best for reducing any artefacts in the stacked image:

Parameter	value
combine	*median*
reject	*avsigclip*
offsets	*shifts.cl*
scale	*mode*
lthresh	-100
hthresh	65536
nlow,nhigh	3
lsigma,hsigma	2.5

Table 3.1: Stacking parameters for the Ks-Band image using IRAF IMCOMBINE

3.5 A quick look on the data

After executing the whole procedure for all three filters, we can already have a quick look on the resulting data, that is going to be basis of the main data-analysis. A preview is shown below:

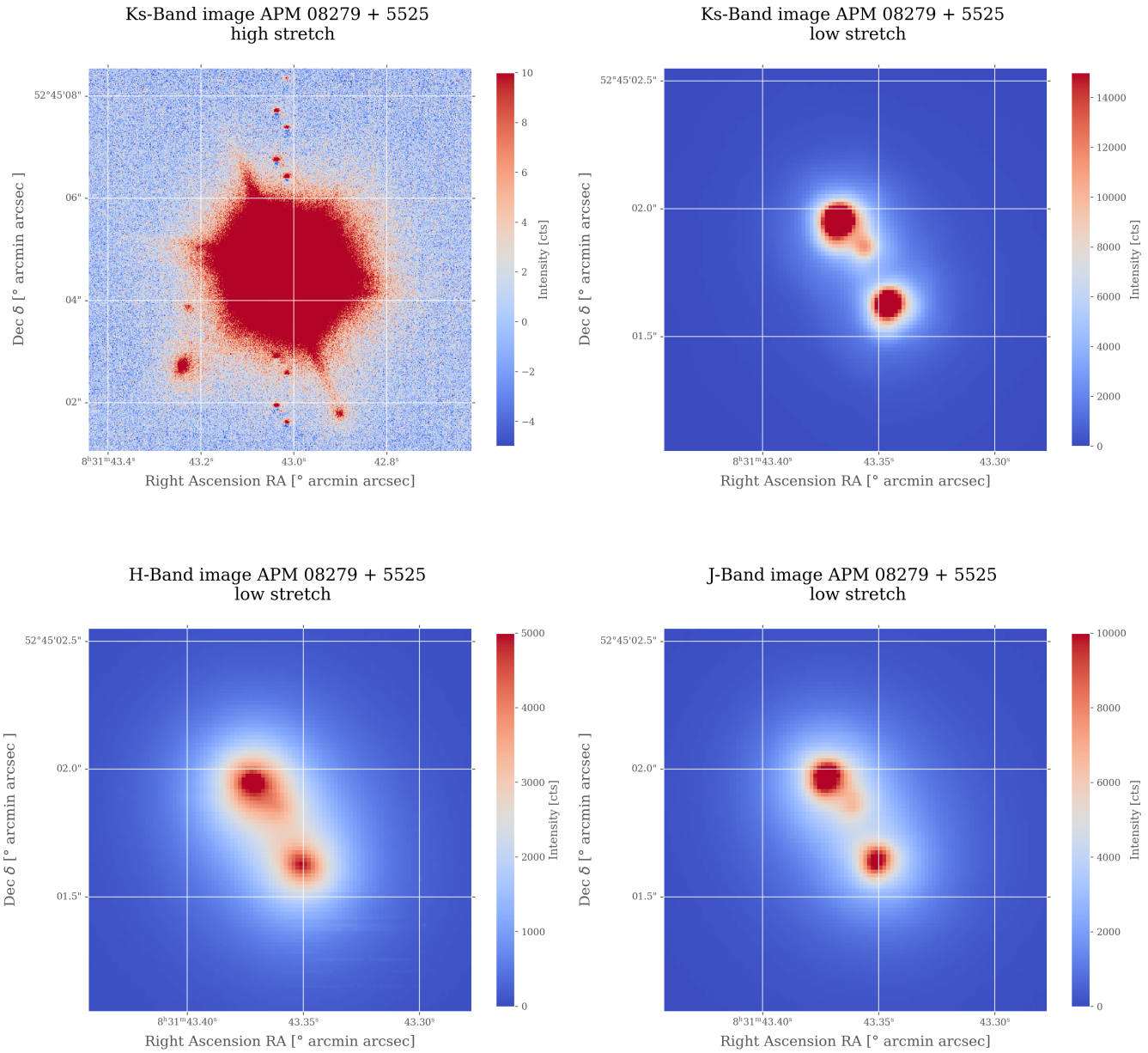

Figure 3.10: AO Observations APM 08279+5255 in the J,H- and Ks-Bands

When quickly examining the stacking results, we can see that the quasar has more distinct components in the Ks-Band image than in the others. The H-Band looks particularily "smeared-out", but all three components are distinguishable without a problem or by PSF modelling/substraction. In the upper left plot at a high histogram stretch, we also see multiple weaker objects in the surroundings of the quasar, as well as a very homogeneous background and some crosstalk artefacts. The J-Band image appears to have a higher strehl value than the H-Band image even though it should have been less favourable to being corrected by the AO.
Another peculiarity about the Ks-Band image is that the 2 brightest components seem to be slighly non-axial-symmetric and appear to be elongated both to the south and east of the brightness peak. This could be either, other unresolved point sources direktly beneath the main brightness peaks, or an erronomous PSF shape created by the AO.

Chapter 4

Calibration and Photometry

4.1 Flux Calibration

Photometric Zeropoints

In order to calibrate the data, or in other words convert values of ADU/cts into photometrical magnitudes, we are going to need additional observations. We are measuring the flux of standartized objects, which are defined to have a certain magnitude and calibrate our data such, that those objects will always have the given magnitudes with our instrumentation. A instrumental magnitude is defined as follows:

$$m_{instr.} = -2.5 \cdot \log_{10}(N[ADU/s]) + m_{ZP} \tag{4.1}$$

Where $N[ADU/s]$ is the number of counts per second of an object and m_{ZP} the so-called Photometrical-zeropoint. It is defined such that it corresponds to the magnitude of one ADU/sec from the object on the detector. It is a definition very similar to the VEGAMAG or ABmag system, however not using a particular star as a reference flux, but a property of the instrumentation.
If we want to compare our measurements to other observatories, the zeropoint has to be calculated from a standartized object such as in our case the HST/NICMOS IR Standard Star BS 9107 [18] converting the magnitudes into the VEGAMAG system.
Under perfect conditions, this wouldnt be necessairy to do when done once for a given set of instruments. But it is always possible that environmental conditions or parameters of the instrumentation undergo changes with time. Solving Eq.4.1 for m_{ZP}:

$$m_{ZP} = m_{instr.} + 2.5 \cdot \log_{10}(N[ADU/s]) \tag{4.2}$$

will let us calculate the zeropoint by measuring the flux and setting m_{instr} to the literature value of BS 9107. The data from BS 9107 was taken in the night from 28th to 29th December 2017 with the LUCI2-instrument as a series of 5 frames 60 seconds (LIR mode with NDIT=6; see section 3.1). Those frames are flatfielded and median-kappa-sigma combined with the *scale = mode* option. Background substraction as in CPT.3 is gratuitous for the demands in this case since the object is

very bright and the background can be taken care of with the flux measurement procedure.
Flux measurement is done by aperture photometry with the Astropy Photutils in the python programming language. It uses the same working principle like the IRAF APPHOT package but makes use of the convenient data-analysis environment python offers.

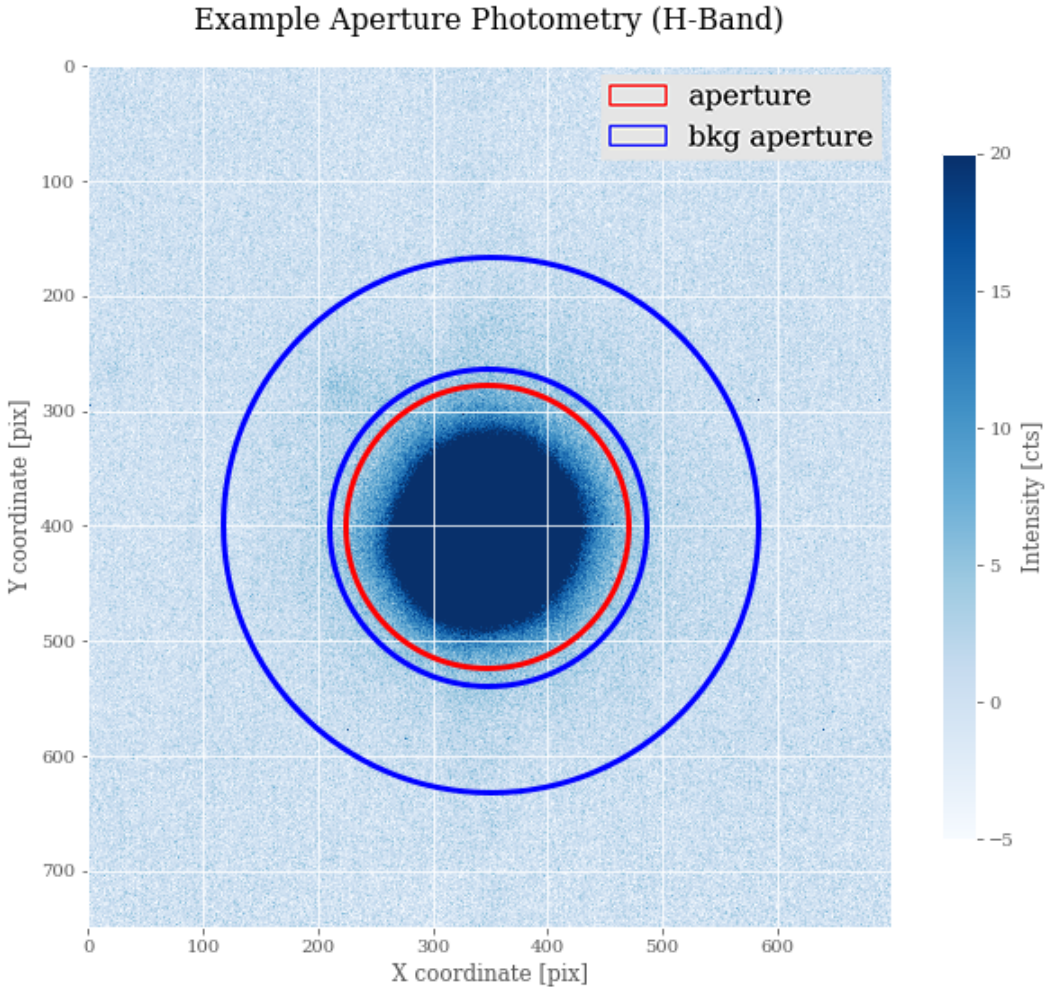

Figure 4.1: working principle of Aperture Photometry

In principle a circular aperture is used to sum up all the ADU of the object substracted by the area-rescaled background obtained from an annulus aperture around the object (see figure 4.1 for visualization). Results for the zeropoints are shown together with the precalculated values from the LUCI-usermanual [5]:

Filter	Calculated value (BS 9107, VEGAMAG)	LUCI-usermanual
J	26.09 ± 0.16	26.34 ± 0.15
H	25.71 ± 0.14	26.02 ± 0.01
Ks	24.90 ± 0.10	25.40 ± 0.01

Table 4.1: Photometric zeropoints calculated for LUCI2 (N30)

Errors are calculated by propagating the poissonian photon shot noise and gaussian background noise (stddev of rescaled background sample). We already see a significant deviation from the literature values, especially in the Ks-Band. Since the AO was not running while taking the exposures, we can exclude strong variations of the PSF and its strehl ratio. Although there is no hint in the observation log, this effect can be caused by anomalous athmospheric absoprtion and variation of the sky background on short timescales (in comparison to the LUCI2 calibration from the manual where the calibration is an average of multiple observing nights [5]).
Zeropoints in the J- and H-Bands are within the 3σ-range of our calculated values. An intrinsic variation of the standart star causing effects of this magnitude is not likely, those stars were especially chosen because of an extremely low variability [18].
This deviation has to be kept in mind when calculating magnitudes of our object, since it directly offsets any photometrical result.

4.2 Photometry of the N30-data: Quasar in J,H,Ks and colors

Having obtained the zeropoints in the section before, we are now able to calculate the apparent magnitudes and colors from the N30-data in the J,H- and Ks-Band and can compare them to values from previous works on this object. Because we are dealing with a multi-image gravitationally lensed quasar whose components are (even in this high resolution data) significantly overlapping, PSF-photometry would by the method of choice in order to calculate the apparent magnitudes for every component from the images. However, due to major problems concerning modelling the PSF (point spread function) this method cannot be applied for our data. This problem is going to be discussed detailed in CPT.5. For this reason we are constrained to use aperture photometry with the limitation of not being able to calculate magnitudes for the components seperately. Similar to Section 4.1 this procedure is performed using the astropy photutils package in python.

Obs.	J	H	Ks	H-Ks	J-Ks
LBT	13.02 ± 0.04	13.08 ± 0.05	11.86 ± 0.03	1.22 ± 0.05	1.16 ± 0.06
Egami et.al.	13.34 ± 0.03	12.65 ± 0.03	12.08 ± 0.03	0.57 ± 0.04	1.26 ± 0.04
SDSS/2MASS	13.41 ± 0.03	12.61 ± 0.03	12.06 ± 0.02	0.55 ± 0.03	1.35 ± 0.04

Table 4.2: Photometrical magnitudes of APM 08279 in comparison

The results unfortunately show significant deviations to previous values for this target. An especially large deviation is seen in the H-Band with the magnitude being a lot higher than expected. This means less Flux than expected is recieved from the target. In the observing log it was meantioned that cirrus clouds were observed during the data aquisition in this particular filter, which could be a possible reason diminishing the flux incident on the detector.
The values for J- and Ks fit better, but are still not within a lower sigma range than 5σ. This suggests that major systematical errors are occuring in our calculations. Significant deviations in the zeropoints from those in the handbook suggest a possible origin in those observations. However if we use those zeropoints only the J-Band result would fit well to the results other observers have obtained.

4.3 Photometry of the N30-data: Deep Field

Another interesting matter at first not having any particular reference to the analysis of the object APM 08279+5255 itself, is to scan the FOV (which is on the contrary very small: 30x30 arcsec) for any interesting objects.
Due to the sparsely populated small FOV, no software aid like the SOURCE EXTRACTOR is needed to identify and list the objects, this is done by-eye and manual collection their coordinates. Additionally we are also performing a quick aperture photometry on the objects found, getting a rough estimate on their magnitude (see table 4.3 and figure 4.2).

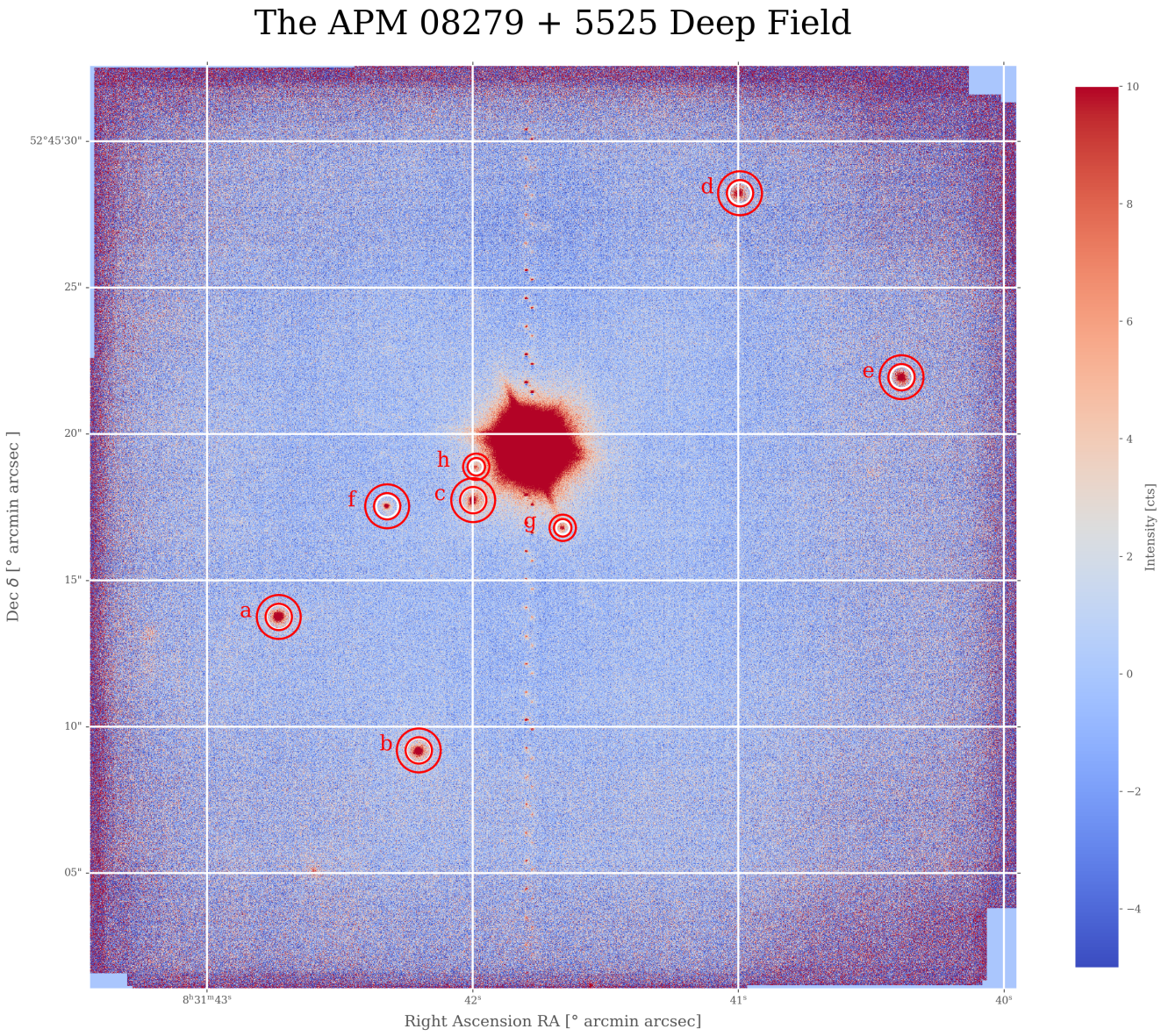

Figure 4.2: Ks-Band N30-data: Deep Field with object identification

This kind of analysis (together with a lot of further steps) can be used to discover possible clusters in the environment of the objects that may give a hint on the existance of a lensing galaxy at approx. the clusters redshift. However the image scale of the N30 camera is not suited that task, the achieved resolution is not as important as the image depth (SNR) (which is mostly important for that matter) of faster systems like the N3.75 Camera. Even though we are using N3.75 ESM-data in CPT.6 for a different purpose than its original objective of a detailed cluster search and analysis, this is outside

the scope of this Bachelors Thesis. The detected objects, their coordinates and Ks-Band magnitudes are shown in Table 4.3:

Obj	X [PIX]	Y [PIX]	Right ascension RA $[h, m, s]$	Declination δ $[deg]$	K_s magnitude $[mag]$
a	431	846	8h31m42.73s	+52°45'13.77	19.54 ± 0.12
b	750	542	8h31m42.20s	+52°45'09.16	19.81 ± 0.13
c	874	1112	8h31m42.00s	+52°45'17.73	20.21 ± 0.14
d	1482	1811	8h31m40.99s	+52°45'28.23	19.94 ± 0.13
e	1850	1392	8h31m40.38s	+52°45'21.91	19.86 ± 0.13
f	678	1098	8h31m42.32s	+52°45'17.54	20.95 ± 0.17
g	1078	1049	8h31m41.66s	+52°45'16.80	21.30 ± 0.19
h	881	1188	8h31m41.99s	+52°45'18.87	22.49 ± 0.26

Table 4.3: Objects of the APM 08279+5255 Deep Field with K_s magnitudes

4.4 A possible 4th component?

By examining figure 4.2 together with Dr. Robert Schmidt (ARI, ZAH Heidelberg), a gravitational lensing expert in modelling complex lensing potentials, we found that a system of Object H together with the known 3 quasar components has a noticable geometrical similarity to other known 4-component objects. This system is illustrated in figure 4.3 below:

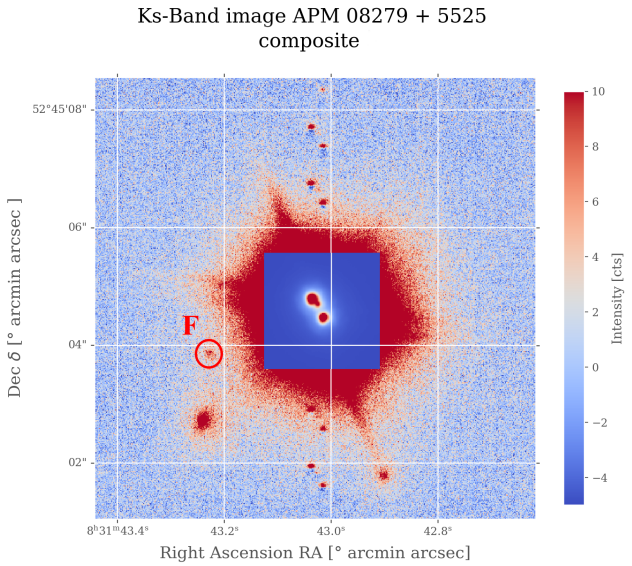

Figure 4.3: A possible 4 component lensing system

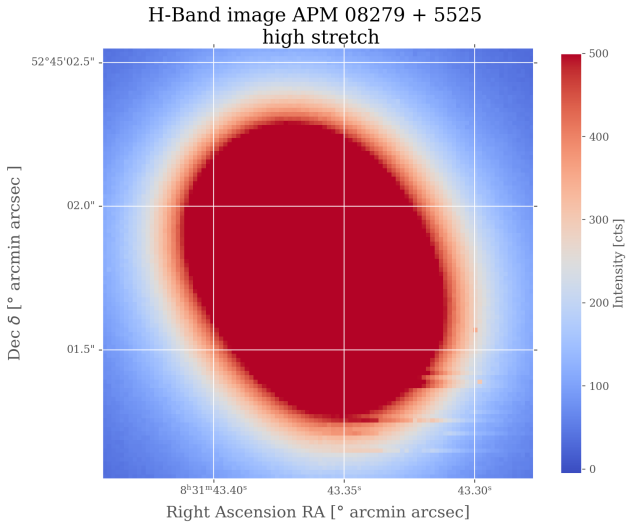

Figure 4.4: Comparison picture in the H-Band

The most striking peculiarity of the potential lensing system is its enourmous brightness contrast, it is rare however not generally ruling out the possibility of creating a reasonable model. Similar objects have already been found and modelled with reasonable results [14], in that particular example it has been concluded that the large brightness contrast was caused by a system of two close galaxies. Since the large brightness contrast of the quasar and Object H does impede a proper visualization of the systems morphology, two different histogram stretches are layered above each other.
To prove the origin of object H being the same quasar as the other 3 components one has to consult other parameters apart from its position, magnitude or resemblance to other systems. The favoured method is to determine colors (astronomically speaking) of an object and compare it to that of the main quasar components. Similar results are a meaningful indication of being another lensing image of the quasar, since under ideal circumstances (neglectic possible differential extinction along the line of sight due to e.g. a lensing galaxy) gravitational lensed images have the same color (see CPT.1 for background).
But note the problematic that can bee seen in fig.4.4, no matter how the minimum and maximum displayed value is chosen, there isn't any structure at the position of Object H to be found. This is most probably because of the extended, "smeared-out" halo hides any other structure. This is also an evidence for a very bad strehl ratio achieved in the observations. If one wants to find any structure the halo has to be modelled by a theoretical profile and substracted similar to CPT.5. This was however not done in this work.
Nevertheless we can estimate the brightness of this object using the colors of the lensed system. Under the assumption that it belongs to the quasar and doesn't suffer from significantly different reddening, we first measure the magnitude of the 4th component by using aperture photometry and then calculate the expected H-Band magnitude.
For the Ks-Band we measure: Ks = 22.49 $\pm$ 0.26 mag at a significance level of $\sim 7\sigma$ above the background. Adopting the gaussian background noise in the H-Band of our data and the color of H-Ks = 1.22 $\pm$ 0.05 it can be calculated that the object's magnitude has to be: H = 23.71 $\pm$ 0.26 mag about 5σ above the background noise. In order to calculated the exposure time needed to achieve this with observations under realistic conditions, (with the LUCI2-instrument) one can use the Exposure Time Calculator on the webpage: http://luci-etc.lbto.org/. We find (assuming a strehl ratio of 0.3 and a sky brightness of 15 mag) an exposure time of minimum $\sim$ 1h 20min for a 5σ significance level. But note two cutbacks of this result, we are using the values obtained in this work which are very likely afflicted by systematical erorrs and assuming no contamination by any other sources. Those are even when achieved to be successfully modelled and substracted contributing residual photon shot noise to the background where component 4 should be detected.

Another estimate one can make from the data available is the position of the lensing galaxy, by only using the relative positions of two pairs of lensed components. Therefore we determine the positions of all 4 components and convert them into dimensionless units, setting component B at the origin of the coordinate system.
We are utilizing the result obtained by Hans J. Witt [10] which constrains the position of the lensing galaxy with an elliptical potential that creates a 4 component system to being on one of two hyperboles. Therefore an java-applet with the help of Dr. Schmidt is used, the hyperboles are rescaled and layered on top of an image of the Ks-Band system:

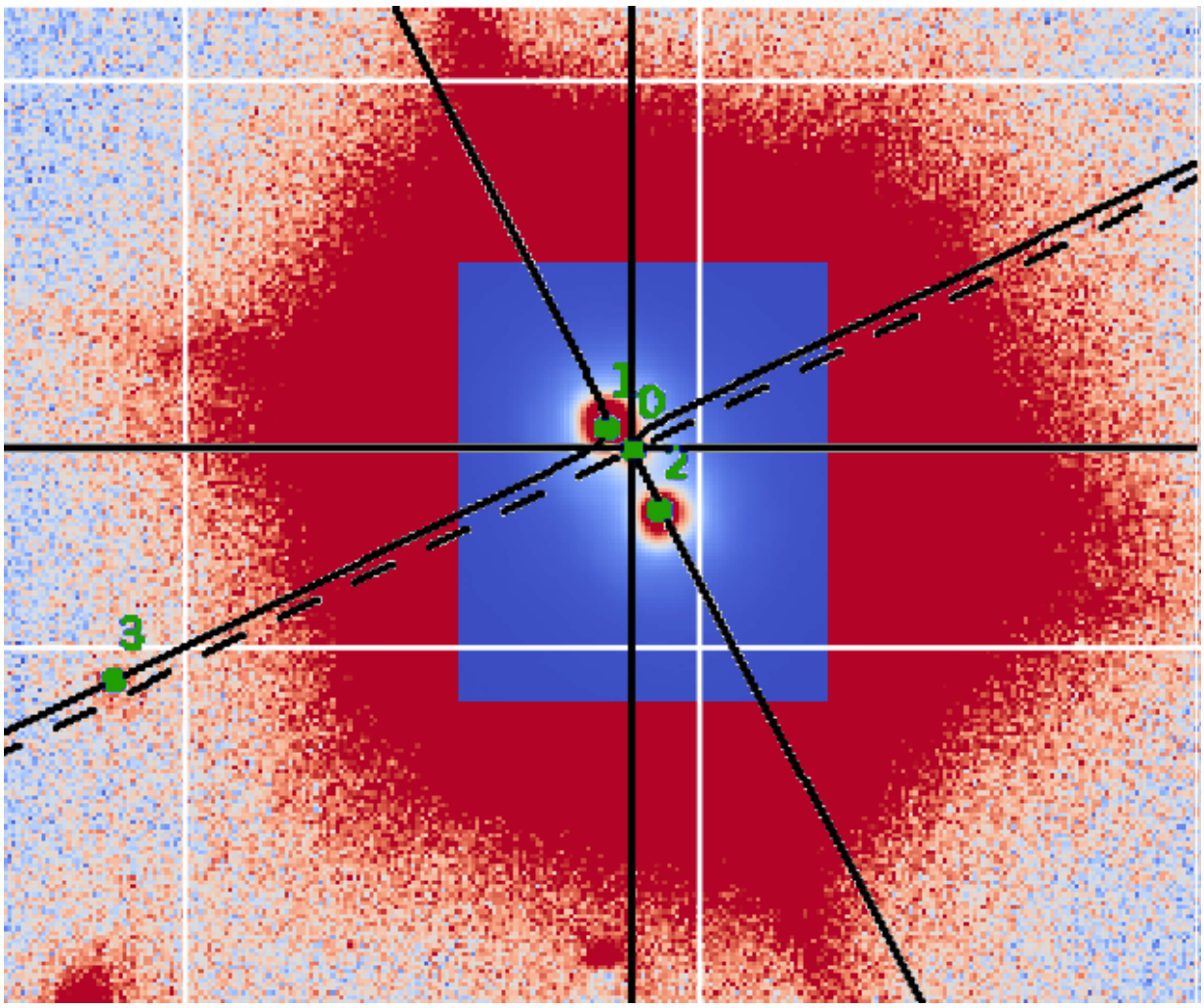

Figure 4.5: A model constraining the lensing galaxy's position

Chapter 5

Structural Analysis

5.1 Basics of PSF fitting

When observing with any optical system, this system as well as any medium along the propagational direction of a wavefront determines the intensity distribution a point source focussed on the detector. This 2-dimensional function is defined as the Point Spread Function PSF. It can be understood as a convolution kernel that is convoluted with the intensity distribution of the source [3]:

$$I(x,y) = \int\int_{-\infty}^{+\infty} I_0(\xi,\eta) PSF(x,y,\xi,\eta) d\xi d\eta \tag{5.1}$$

or in short: $I(x,y) = I_0 * PSF$. If the telescope uses a circular aperture of diameter D, the PSF is given by the diffraction limiting Airy disc:

$$PSF_D(r) = \frac{1}{\pi}[J_1(br)/r]^2 \qquad \text{where} \qquad b = D\pi/\lambda f \tag{5.2}$$

With a fixed observed wavelength λ, focal length f and diameter D the Airy-disk can be only described by a single parameter in the focal plane, the radius resulting in radial symmetry.
Due to athmospheric turbulence the PSF does not have this idealized shape in real observations. It is a combination of the Airy disk and a radial-symmetric 2d-Gaussian profile induced by the athmosphere:

$$PSF_s(r) = \frac{1}{2\pi s_0^2} \exp(-r^2/2s_0^2) \tag{5.3}$$

Here s_0 quantifies the seeing (short term for the effects of athmospheric turbulence on the wavefronts of incoming light) as the FWHM of the distribution. If the PSF resembles a profile of this shape one talks about seeing limited observations.
The profile (which is typical for AO observations) can be well described by the Airy disc superposed with the so-called Moffat profiles:

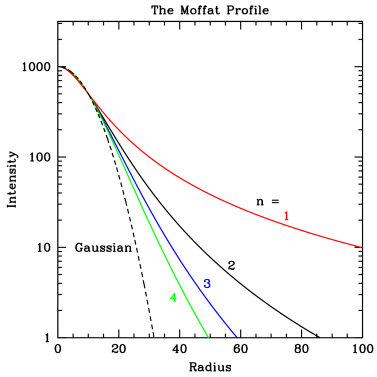

Figure 5.1: Radial Moffat profiles

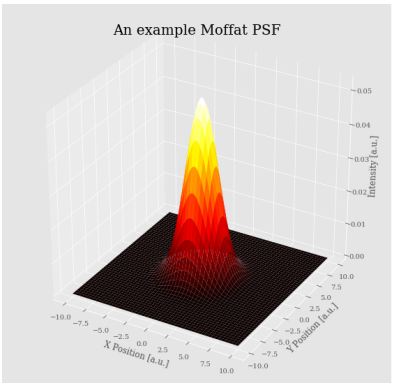

Figure 5.2: An example 2D Moffat PSF

Its profile is described as follows:

$$\Sigma(r) = \frac{\Sigma_0}{[1 + (r/r_d)^2]^n} \qquad \text{with} \qquad r_d = \frac{\text{FWHM}}{2\sqrt{2^{1/n} - 1}} \tag{5.4}$$

Where n is a parameter describing the "steepness" of the profile and r_d a characteristic radius. If one wants to recover information about the system before PSF-Convolution, especially when individual point-sources are not well resolved, a technique calles PSF-Fitting can be used. Based on a χ^2-optimization process, a model of the intensity distribution by fitting the PSF profile to every source, determining its total magnitude and position, since those are the only free parameters of a PSF.
This however only works if the sometimes complex shape of the PSF the optical system creates can be extracted from the imaging data or modelled very accurately by fitting a special 2D-profile (like the Moffat profile in fig. 5.2). The model can then be substracted from the object to be fit in order to obtain a residual (see fig.5.3) that can be examined to review the fit and spot errors of the model.

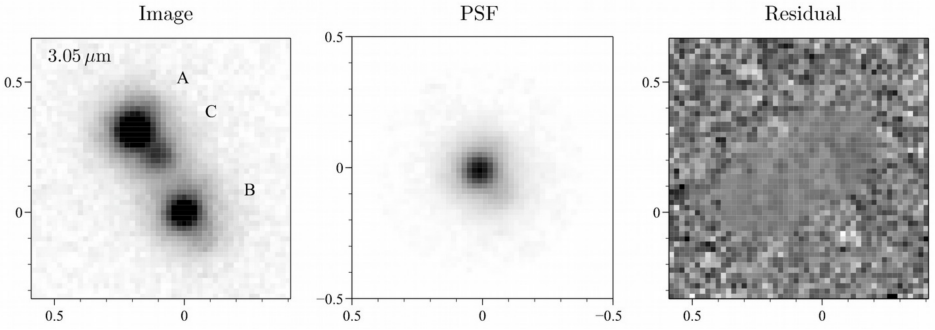

Figure 5.3: PSF-fitting process as executed by Oya et.al [19]

The software of choice to adress this task is the 2D-Profile fitting tool GALFIT by C.Y.Peng [12]. It features a wide range of different profiles and the option of using external images as a PSF to

be fitted to the data. The input can be controlled by a special input file, denoting all profiles fitted simultaneously with their initial expected values. Those can be either fixed or free and to be dtermined by the fitting procedure.
If the fit is successful an fits-imageblock is returned, containing the object itself, a model and the residual in its extensions. Those can be easily opened using DS9 or the astropy FITS package.
We now want to utilise this tool for creating a model of the 3 known QSO components, estimate their positions and magnitudes as well as substracting the model from the data in order to search for previously covered or unsresolved structures. These could for example be a lensing galaxy or more components of the lensed QSO.

5.2 Simple Moffat profile

The first approach to obtain a model for the 3 Quasar components is to use a fairly simple analytical profile, the Moffat profile as a PSF. However its shape parameters are still to be determined in the fit. Additionally galfit can modify the radial symmetric profiles to an ellipsoidal shape using the axis ratio b/a of the two major axes and their position angle θ with respect to "UP" in the image.

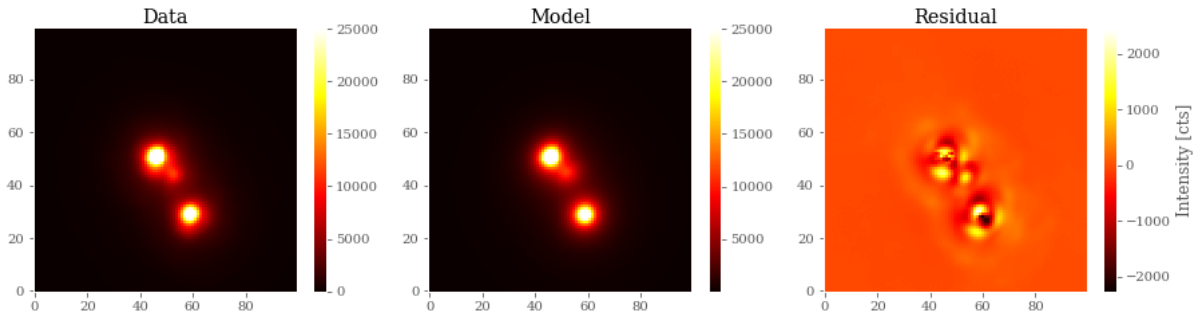

Figure 5.4: A model using Moffat profiles

After numerous iterations with different starting parameters for the fit we get this rather disappointing result:

Comp.	X [px]	Y [px]	Ks [mag]	FWHM [px]	n [a.u.]	a/b	θ [deg]
A	246.99	251.65	13.22	5.79	1.38	0.91	-38.19
C	253.60	245.26	14.44	8.57	1.50	0.89	-36.70
B	260.23	229.72	12.79	5.81	1.17	0.97	-23.81

Table 5.1: Fitting results Moffat-fit

In order to analyse the quality of the fits not only the χ^2/dof value is important, also the residuals are a very useful tool. We can calculate quantities such as the mode, minimum and maximum value,

to gauge a general over- or undersubstraction. Also the following quantity can be of interest to estimate the quality of the fit:

$$P = \frac{sum(|I_{residual} - I_{median}|)}{sum(I_{object})} \tag{5.5}$$

That is basically the percentage of total deviation in Flux of the model from the original data, where we substracted the median before in order to not count any general over- or undersubstraction. If we analyse the residual in this way we can obtain the follwing values:

min [ADU]	max [ADU]	mode [ADU]	χ^2 / dof	P
2261	2453	-2.649	41.361	0.115

Table 5.2: Analysis of the residual for the Moffat fit

We see no really significant over- or undersubstraction in the total frame, but one can clearly see that around the peaks of the model profiles, the residual shows conspicious structures of a bad modelling. There are small patches of over- and undersubstraction that occur in similar patterns fot the A and B components. The bottom and the right of the peaks surroundings show undersubstraction (image brighter than average) which corresponds to an assymmetrical extend of the source in those two directions, deviating from a simple elliptical shape. The center of the sources show a significant oversubstraction or are generally speaking not modelled well at all. This might be due to the fact that a PSF profile of AO supported observations is normally a composition out of a moffat profile describing the outer regions of the peak and a Airy disk describing the very center. This of course cannot be modelled very precisely by a Moffat profile alone and requires modelling another overlaying function or external PSF. Also no matter how well all the other parameters are fitted disrispectly of the radial profile shape, there's always going to be significant residual structures, since the complex azimuthal shape of our PSF profile cannot be described by the limited azimuthal degrees of freedom of an ellipse. This would require using additional GALFIT fitting options such as *Azimuthal fourier modes* or the *diskiness/boxiness* parameter created for fitting in partical elliptical galaxies. However this lies outside the scope of this work and might be conducted by follow up research.
We also performed a quick research on the question whether this assymmetry is an artefact caused by the data-reduction process (e.g. has been created by inaccurate alignment of the individual frames or excessive rejection). This has been carried out by analysing several samples of difference frames from individual frames in the series of the integration. However no significant trend in the resulting structures showed up, indicating a systematical error ontop of any intrinsic variations of the PSF. Also average stacks without any rejection have been performed, whose differences to the actual stack dont show any suspicious structure.
We are now going to follow the approach of using such an external PSF.

5.3 Synthetic PSF models

Another idea for modelling the system is to use an external PSF for fitting, as described before. This is a fixed 2D profile aiming at representing the image of a point source by the optics and line-of-sight effects.
This PSF of fixed shape has to be obtained seperate from the fitting process. The most common approach is to scan the FOV for other point-sources (like e.g. stars or distant QSOs) and use their intensity profile as a PSF for modelling the object of interest. However, this also requires a number of preconditions to be met. A common problem with AO-supported observations is that the PSF is highly variable in time and dependant on the position in the FOV (normally one defines an so-called "isoplanaic angle" in which it is assumed to be spatially constant) and the observational conditions. We therefore require our "PSF-source" to be observed in the same timespan and in the same FOV. When doing stellar PSF-modelling in crowded fields like star clusters, this doesn't pose much of a problem choosing some stars in the isoplanaic angle for creating the PSF. But in our case the FOV is almost devoid of any other objects that are both sufficiently point-like and bright enough to being used as a PSF model.
Since additional observations of e.g. some stars for modelling the PSF will not represent the PSF under the conditions of the main observations, we have no other choice than to extract a PSF model from the object itself. This is obviously a challenging task regarding the little angular seperation and strong overlap (especially in the bright halo complete object). Nevertheless we will give it a try using similar techniques to Egami et.al. [9].
For a system of this morphology, we follow two different approaches to create a sysnthetic PSF model and examine their fits to the object. This will also adress problems with the assymmetry of the component's PSF. The idea is to use components A and B, respectively the least overlap and halo compromised parts of it for creating the models. The easiest way to seperate the components is to slice them along a vertical line (parallel to the y-axis) trough their center of brightness (see fig. 5.6), this also doesn't require any linear transformations or rotations applied to the PSF-slices for reconstruction. But first we want to diminish the overlap of components A and B with each other and component C. Therefore we fit component A and C with component B and subtract to isolate component B. Additionally component B is fitted with component A, where component C has already been substracted after beeing modelled by component B. We can see the resulting images of component A respective component B below (fig. 5.5):

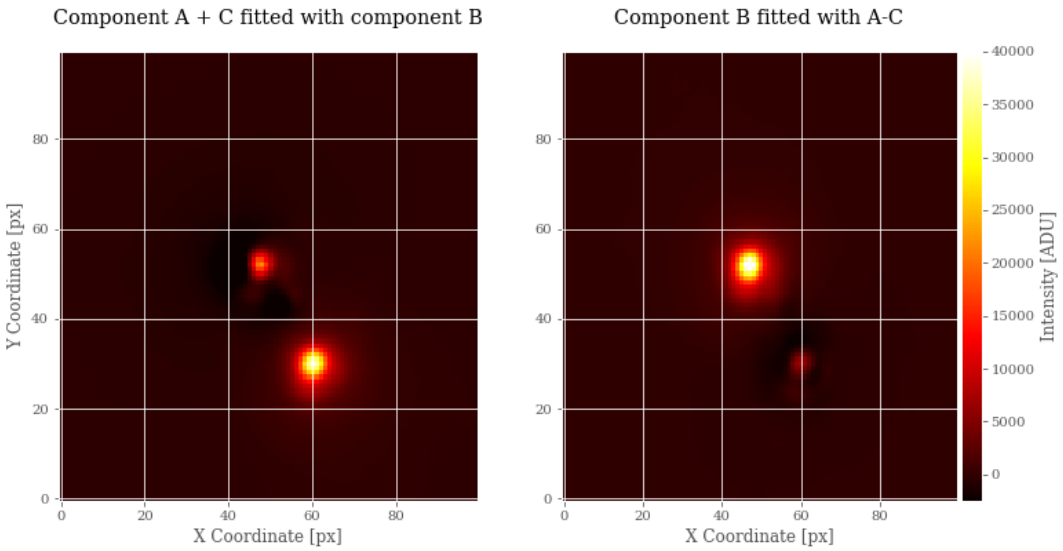

Figure 5.5: An attempt to isolate components B and A from themselves

Now we can slice the components to create our PSF models.

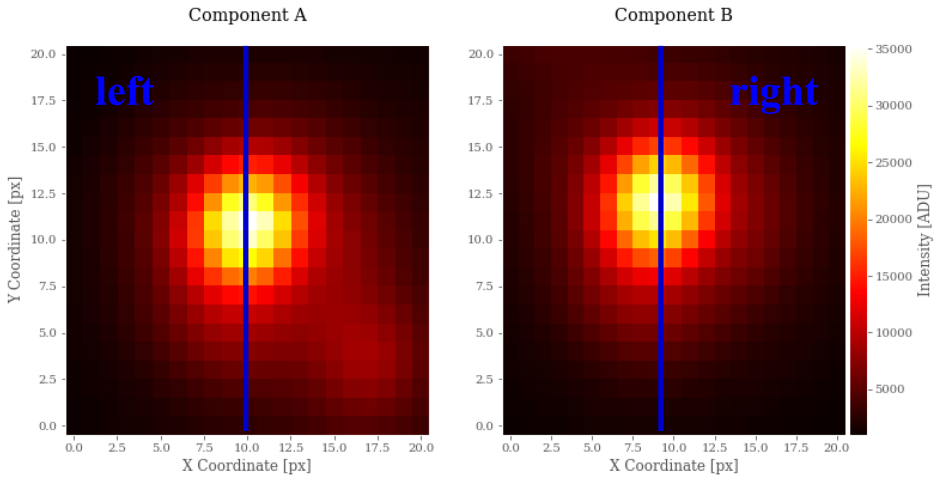

Figure 5.6: Components A and B are to be sliced for PSF modelling

This procedure as well as the reconstruction are executed in python using the NUMPY module. We can use the left slice of component A and the right slice of component B.

5.3.1 Merged PSF

In this approach we are stitching together both halves of the components for a combined model. However both components have different total brightnesses and have to be aligned with each other. The shift can simply be calculated by using the SCIPY PEAKFINDER algorithmus on both vertical profiles. For rescaling we are using the property of the PSF (in theory) only having one other free parameter, the total brightness. This is calculated by numerical integration of both profiles, resulting in a simple factor for rescaling (see fig. 5.7):

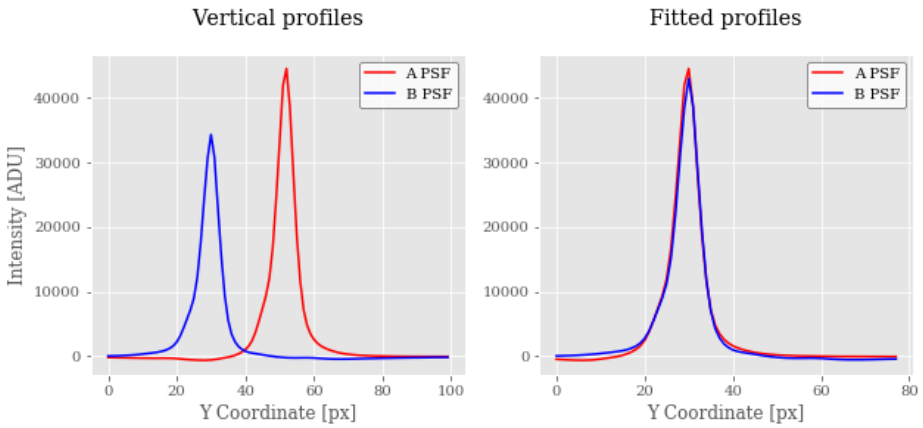

Figure 5.7: Shifting and aligning both slices

Now both halves can be recombined and the resulting model can be used for the PSF fits. This model should account for the assymmetry of the PSF, it assumes neither radial nor axial symmetry.

5.3.2 Mirrored PSF

The second much simpler approach is assuming an axisymmetric PSF with respect to the vertical axis through the center of brightness. This allows us to mirror both of the slices to create axisymmetric models of A and B. Averaging both models will better account for any smaller morphological differences of both components.

5.3.3 Fitting results

After executing PSF fits with both synthetical PSF models we are analysing the results:

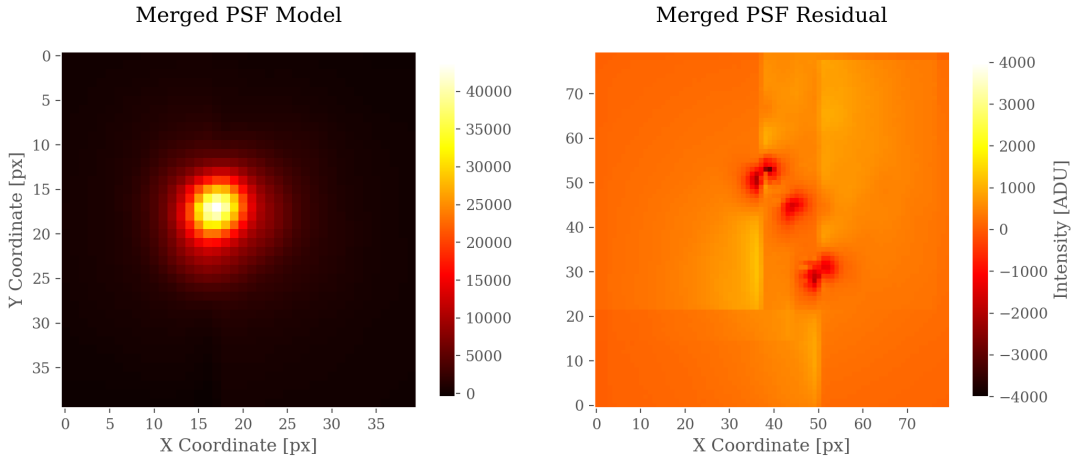

Figure 5.8: merged PSF model and residual of the fit

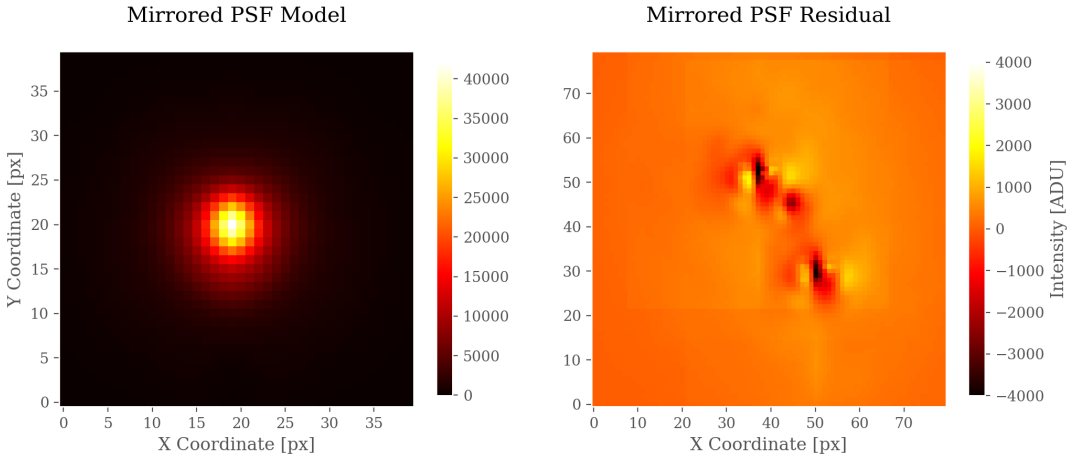

Figure 5.9: mirrored PSF model and residual of the fit

For the magnitudes and positions of the 3 components, we obtain the following values (note that positions had to be shifted from the output of galfit since the PSFs center of brightness was both times not in the center of the PSF fits frame):

PSF	Comp.	X [px]	Y [px]	Ks [mag]
Merged	A	247.01	251.91	13.07
	C	254.09	245.71	14.75
	B	260.11	230.10	13.35
Mirrored	A	247.08	251.95	13.03
	C	254.43	245.08	14.66
	B	260.17	231.10	13.29

Table 5.3: Fitting results Synthetic PSFs

If we analyze the residuals in the same way as before we get:

PSF	min [ADU]	max [ADU]	mode [ADU]	χ^2 / dof	P
merged	2883	1241	0.582	313.031	0.258
mirrored	4480	1893	5.424	280.314	0.248

Table 5.4: Analysis of the residuals for the synthetic PSF fits

We see that rating by the χ^2 / dof and P value, the mirrored PSF has produced a better result. But this conclusion is not that easy to be made, both measurements are related to the deviations of the pixel values in the model from those of the data over the whole data-set. We can clearly see, that the fits from the merged PSF show smaller residual "bumps" in brightness, but a strong artefact from different background gradients in the recombination process of the two different halves. This is espected not to have an influence on the mirrored PSF, since there are by construction no different values at the "seam" of both halves. However, in order to smoothen this effect for the merged PSF without influencing the brightness peak is very difficult.
Just argumenting based on the visual appearence and min, max and mode values (min,max should be as small as possible and mode ≈ 0) the merged PSF would do a better job, as expected since it is able, by not having assumed any symmetry, to cover a higher degree of assymmetry.

Chapter 6

ESM Data

6.1 Data reduction

The data-set that is going to be discussed in this chapter was taken by the N3.75 camera of the LUCI2 instrument in the night from February 12th to February 13th. It was primarily intended to analyse the environment of the quasar APM 08279+5255 in its 4x4 arcmin FOV to search for any signs of a galaxy cluster at a lower redshift than the quasar, which could host a possible lensing galaxy for the complex gravitational lensing system of the object. A total of 107 mins a 60 sec subframes have been aquired in both Ks- and H-Band. These observations use the Enhanced-Seeing-Mode ESM, which corrects for a couple of lower order zernike modes and tip-tilt abberation on a larger pixel-scale of $\sim$ 0.12 arcsec/pix . Comparing to observations with the N30 camera and full-AO mode, this can be seen as a sacrifice of resolution to gain a significantly higher SNR and larger FOV. Consequently these observations are better suited to detect faint sources in the field than a detailed structural analysis of the quasar. However they respresent a good possibiliy to perform some consistency checks and verification of results from the N30 data. Data-Reduction has been executed with a very similar procedure to the one used for the N30 observations. Since the underlying process and reasoning has been described fairly detailed in CPT.3 we are going to skip the discussion of this step. The resulting integrated images in Ks- and H-Band are shown below (figure 6.1 and 6.2).

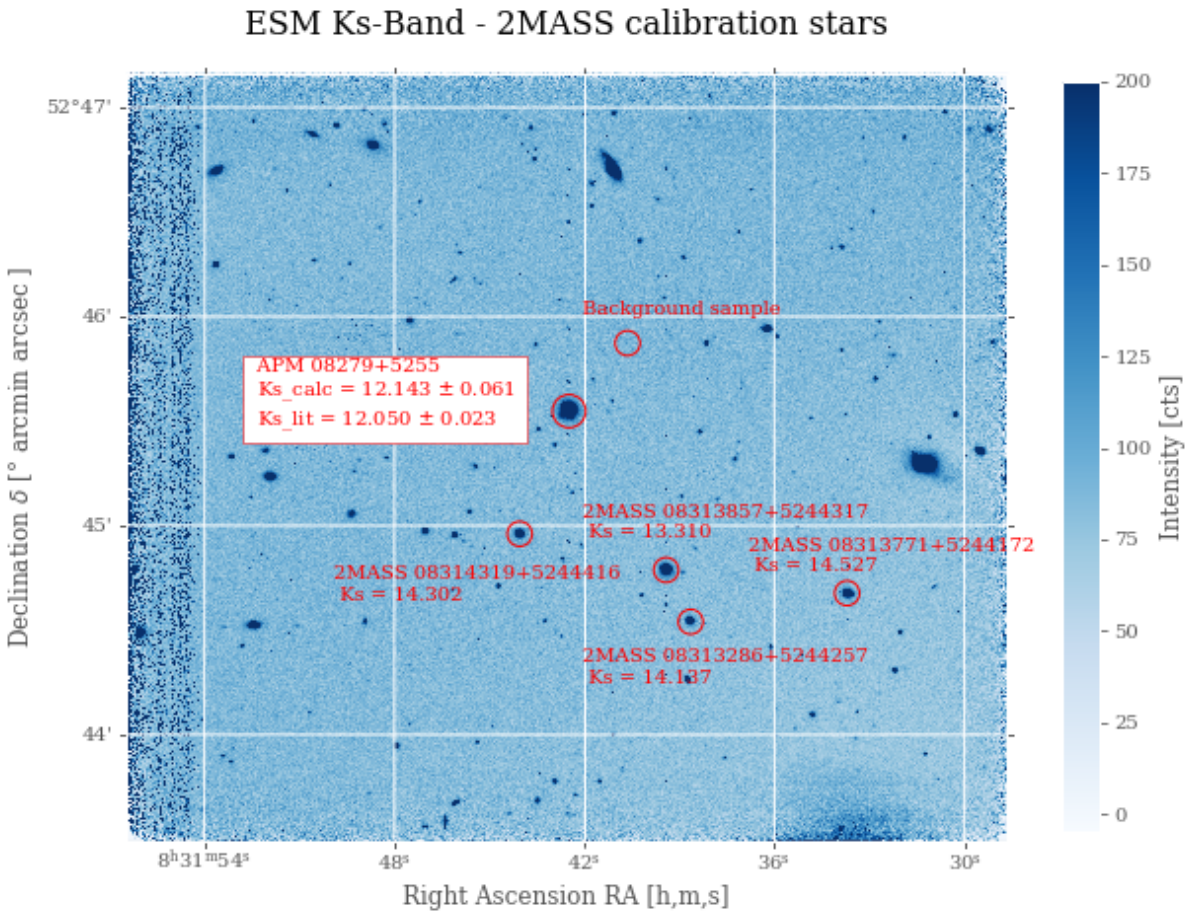

Figure 6.1: ESM Ks-Band image with photometry and calibration

The quasar is located just in the center of the FOV. In the Graphics are already marked the positions and magnitudes of objects that are important for the next section.

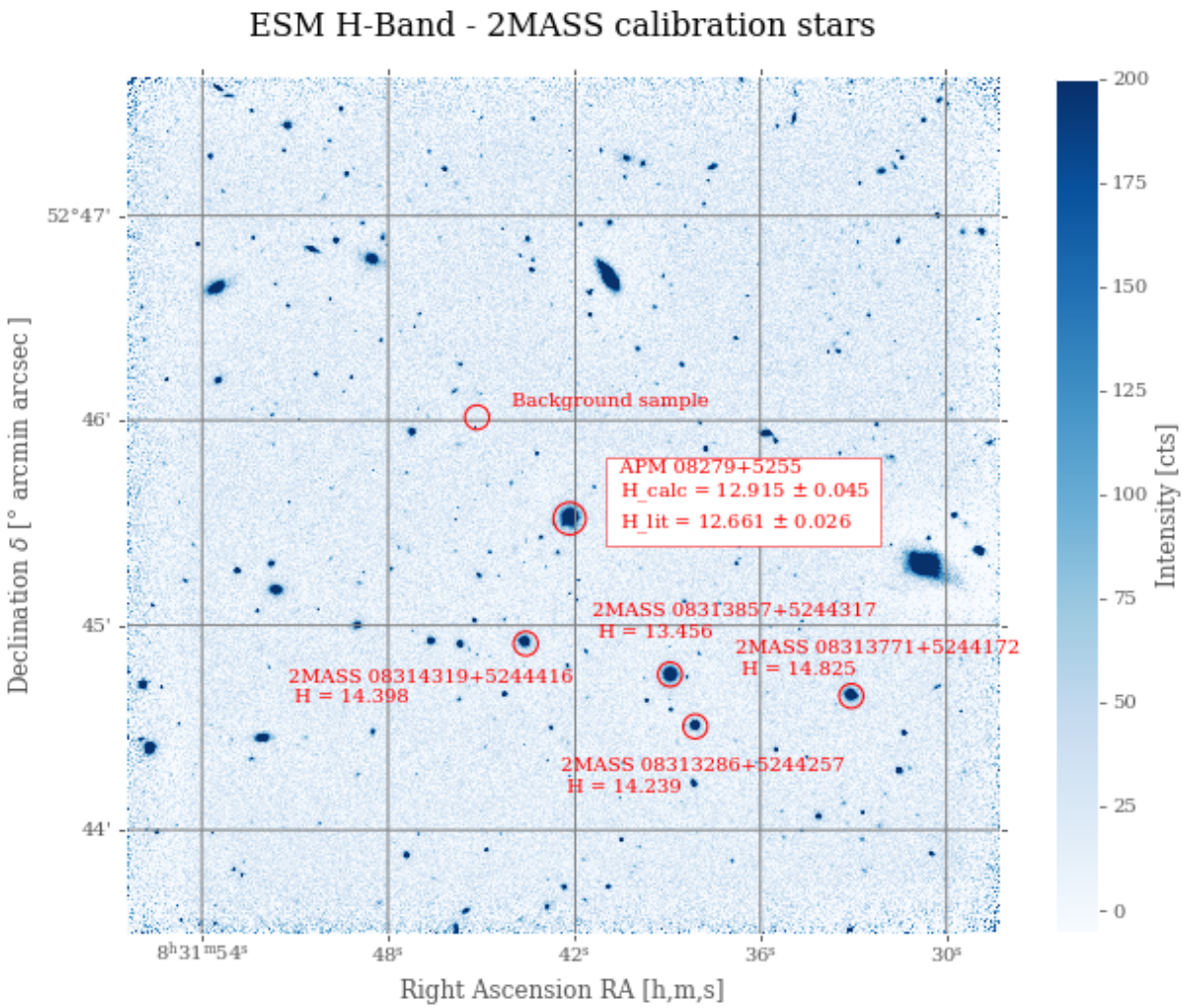

Figure 6.2: ESM Ks-Band image with photometry and calibration

6.2 Calibration

In contrary to CPT.4 due to the comparably large FOV, we are now given the opportunity to calibrate the flux with the help of 2MASS objects in the fields. For this purpose we are scanning the 2MASS catalogue [15] in a simbad search in the area encircled by a radius of 4 arcmin. This gives us a couple of (point)-sources that have magnitudes suitable for a flux calibration. This works very similar to the flux calibration executed in CPT.4, however the zeropoints are not calculated from a Persson NIR standard star but from the 2MASS field objects with the same formula (eq. 4.2) applied. Since we are calculating for multiple objects, the result and error of measurement will be the average and

stddev respectively. For comparison, the instrumental magnitudes of the objects calculated with the LUCI2 zeropoints from [5] and the instrumental magnitudes calculated from 2MASS are shown in figure 6.3.

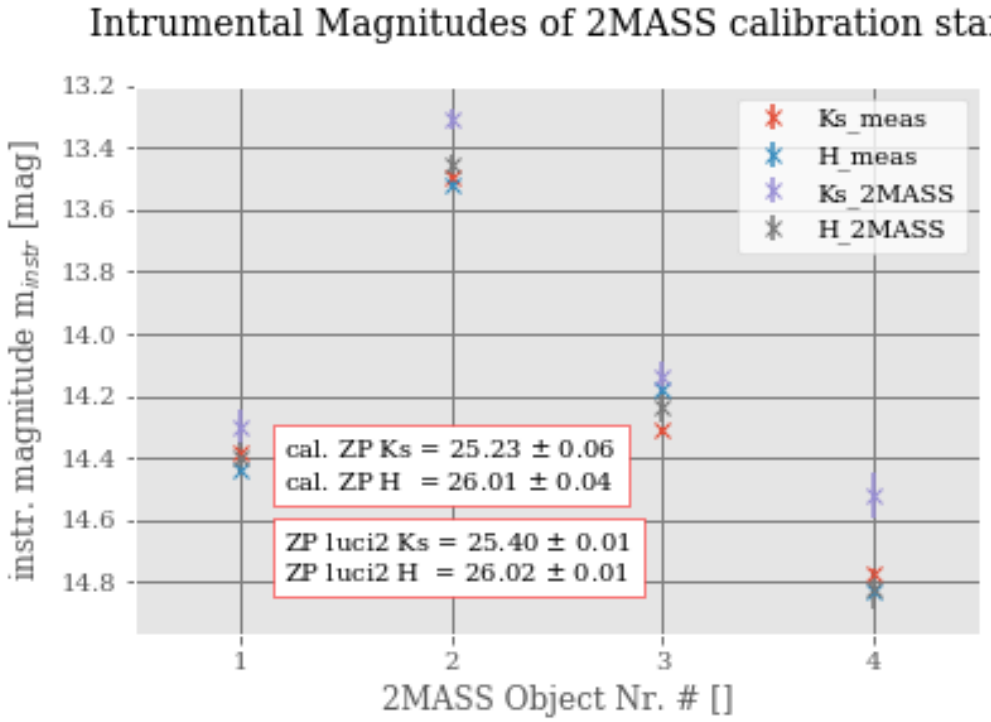

Figure 6.3: Zeropoint Calibration

6.3 Photometry of the quasar and 4th component

Although the PSF-shape is expected to be much less of a problem compared to the N30 data discussed in CPT.5 we are not going to perform PSF-photometry with this data. Aperture photometry should give a good estimate of the quasars total luminosity since its not resolved into the individual components anyways. A meticulous modelling of the quasar might show a double structure and reasonable magnitued for the individual components, but however this is outside the scope for the ESM datas purpose in this work. Using the 2MASS calculated zeropoints we can estimate the H- and Ks-Band magnitudes. Via aperture photometry we find (the results are also shown in figure 6.1 respectively 6.2):

Filter	N30 (BS 9107, VEGAMAG)	N3.75 (2MASS, VEGAMAG)	LUCI-usermanual
J	26.09 ± 0.16	—	26.34 ± 0.15
H	25.71 ± 0.14	26.01 ± 0.04	26.02 ± 0.01
Ks	24.90 ± 0.10	25.23 ± 0.06	25.40 ± 0.01

Table 6.1: Photometric zeropoints calculated for LUCI2 (N30 and N3.75)

We quickly notice that the zeropoints calculated with the 2MASS catalogue are fitting to the zeropoints from the LUCI-usermanual a lot better than those calculated with the N30 camera. Those photometric zeropoints are also much less prone to the statistical errors inheritant of the calculating procedure, since a dataset of much longer exposure time and multiple objects are used. This also refelcts in the smaller error ranges obtained.
When comparing the Quasar's mangitudes in the H- and Ks-Band we notice that they deviate from the literature results by more than 5σ. There must definetly exist some systematic errors in the data or the calculation of the values, due to the good agreement of the zeropoints we don't suspect them to be the source of error. Another possibility is the occurence of microlensing effects or emission line variability such as described in [22], that have been already observed, however not in this magnitude.

6.4 Comparison of photometrical values

Using aperture photometry and PSF fitting for the N30 and aperture photometry for the N3.75 ESM-data we can now compare the photometrical resuts from different approaches and datasets. When using aperture photometry the QSO was not resolved and the flux measured as originating from a single source. For the magnitude of the individual components we therefore use the flux ratios measured by Egami et.al. [9] from figure 1.5. Magnitudes from the individual components are always measured in the Ks-Band. Also error ranges are not included, they range from ± 0.01 to ± 0.06 mag in those data-sets and can be looked up in the individual tables from CPT.4 and CPT.5.

Dataset	Method	A	B	C	J total	H total	Ks total
N30	Ap-phot	12.60	12.87	14.33	13.02	13.08	11.86
N30	PSF (Moffat)	13.22	12.79	14.44	—	—	12.10
N0	PSF (Merged)	13.07	13.35	14.75	—	—	12.33
N30	PSF (Mirrored)	13.03	13.29	14.66	—	—	12.27
Egami	PSF	12.82	13.09	14.55	13.34	12.62	12.08
N3.75	Ap-phot	12.89	13.15	14.62	—	12.92	12.14

Table 6.2: Comparison of all photometrical magnitudes for the 3 component system

From this we can conclude that the photometrical values from the PSF Moffat fits and the ESM-data are closest to those previously observed by Egami et.al. [9]. For the other PSF fitting methods, deviating results for the individual components and a a general under estimation of the total magnitude

is observed. A more detailed analysis of the individual approaches and the conclusions as well as error analysis is conducted in the individual sections.

6.5 Deconcolution and morphological analysis

As we already mentioned, every point source in an astronomical image is convoluted with the Point-Spread function (defined by seeing and/or the optical system), limiting the resolution achievable. As we have seen in the data taken by the N30 camera with the support of full-AO mode, this PSF can be sufficiently narrow for being able to easily resolve the 3 individual confirmed quasar components and the possible 4th component in the Ks-Band. However the ESM only corrects a couple of zernike modes and is working on a completely different pixel-scale of the N3.75 Camera. This generates a significantly higher SNR at the expense of resolution.
If we want to resolve some structure in the object using this data, we need to consult other data-analysis techniques: The Richardson-Lucy Deconvolution is a iterative numerical technique that aims to reverse the effect of PSF convolution to a limited degree and can be applied to well sampled, high SNR data like our ESM-data (see figure 6.4). We are just interested in confirmation that an object exists at the predicted position for the possible 4th component found in the N30 data and hence do not care about conserving flux for further photometrical analysis.

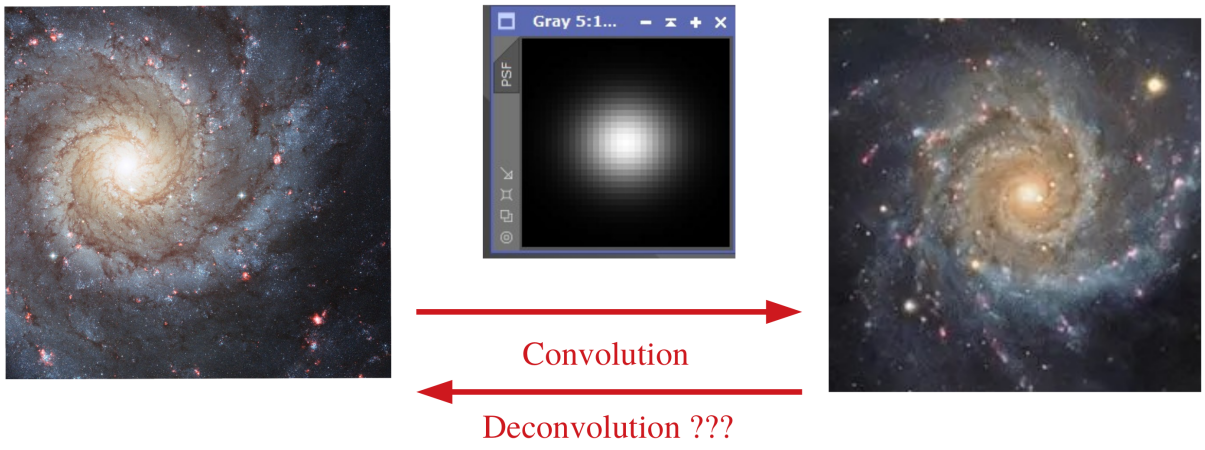

Figure 6.4: The idea behind Deconvolution

To conduct a deconvolution process one first has to create a model of the PSF. In case of the ESM data we dont have the problem as in CPT.5 of a small FOV without point-sources of decent SNR. We are now able to use a number of stars in the FOV to model the PSF needed for the deconvolution. Because of pracitcability another software is used: Pixinsight. This software package dedicated to image-manipulation and analysis, offers an easy-to-use graphical interface to choose stars and the model used to create a PSF.

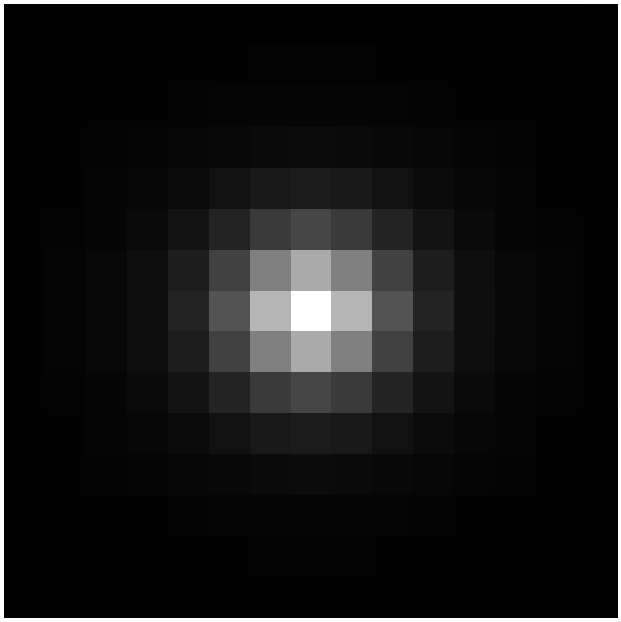

Figure 6.5: PSF model Ks-Band

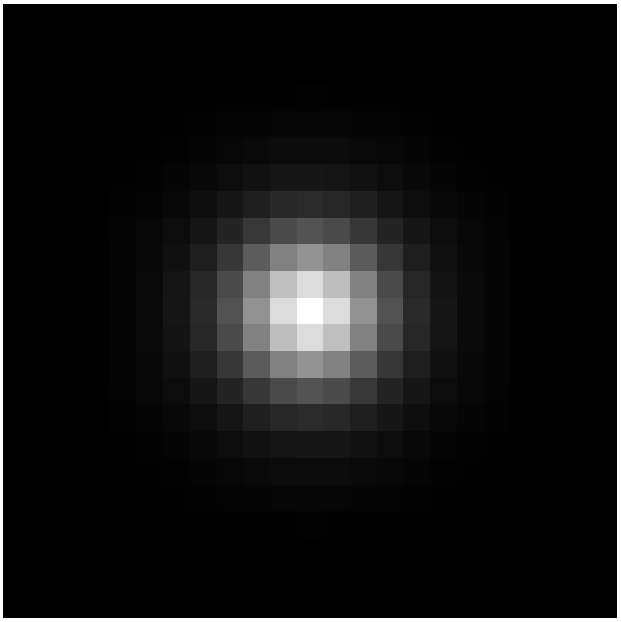

Figure 6.6: PSF model H-Band

The deconvolution process can also be executed with this software. A convienent advantage is that it is possible to create variable preview windows on the image, not needing to execute the CPU intensive and slow process on the whole data. The most important parameter are the iterations, a higher number will result in a stronger effect of the deconvolution while also producing more artefacts. It is very common that deconvolution produces ring-like ("Gibbs-effect") artefacs in areas of high contrast, such as stars or other point-sources. If one wants to make robust scientific conclusions, those artefacts have to be avoided as much as possible or corrected with special filtering algorithms ("deringing" algorithms).
After a couple of attempts, we find that the best results, i.e. those that produce the least ringing artefacts while still showing a satisfactory effect, are achieved when choosing about 50 iterations. Results of the deconvolution applied to the Ks- and H-Band ESM images are shown in the figure below.

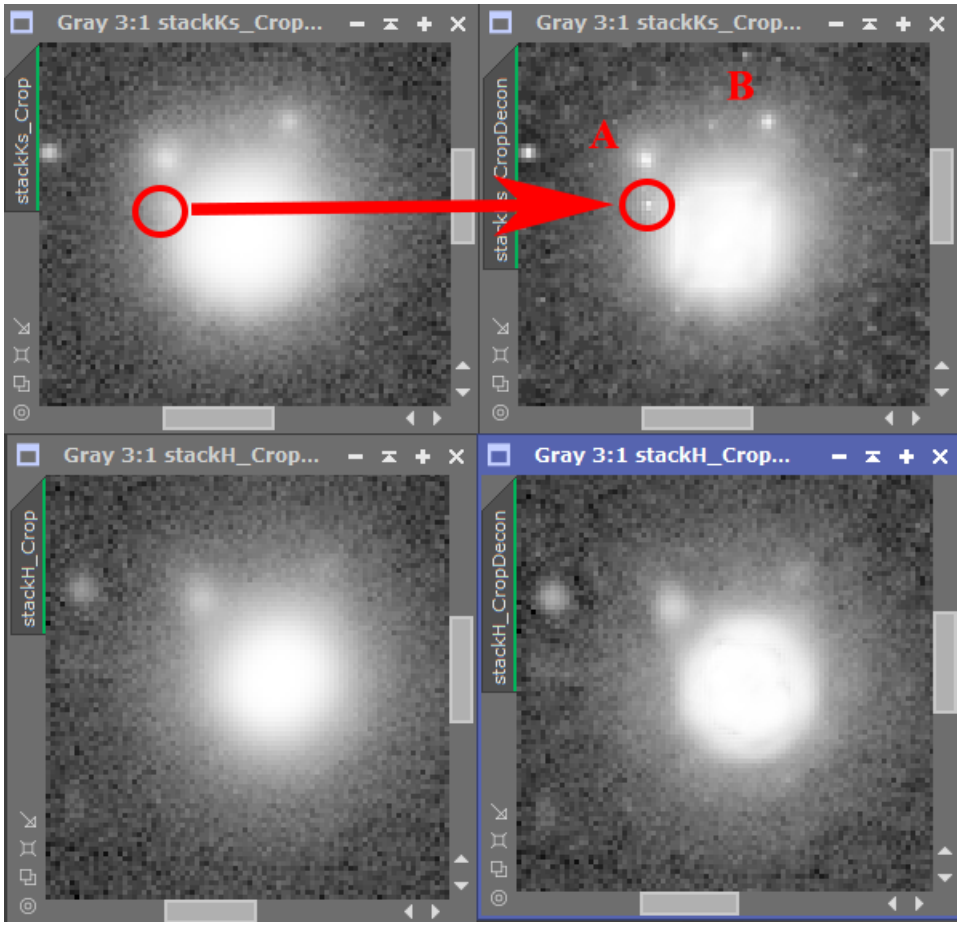

Figure 6.7: Deconvolution of the ESM-data

We quickly notice, that in the Ks-Band a small but distinct brightness peak occurs in the outer halo of the quasar. This could be the possible 4th component seen in the N30 data. However we want to check this assumption by calculation of the distance to the next two objects in the field. We are intentionally not calculating the distance to the quasars luminosity peak since this measurement can be ambigious on a not or partially resolved double peak from the 2 brightest components in the ESM data. For the calculation we use Objects C and G from the N30 deep field analysis (see figure 4.2), that are also well visible in the ESM-data. The brightness peaks positions from the objects are calculated with the IRAF STARFIND command.

Dataset	Pixelscale [arcsec/pix]	d_a [arcsec]	d_b [arcsec]
N30	0.015	1.160 ± 0.042	3.637 ± 0.042
N3.75	0.118	1.162 ± 0.083	3.567 ± 0.083

Table 6.3: Geometrical measurements for component 4

We see that for both distances, the more accurate determination from the N30 data lies well into the 1 sigma error range of the less accurate distance calculations from the N3.75 data. This highly supports the claim that it is the same object visible in both independent data-sets and therefore renders the possibility of the object just being a random artefacts in one of the data-sets highly unlikely. However this does not tell anything about the question whether the 4th really is a 4th component of the quasar and not another independent uncorrelated source in the field. Unfortunately we cannot see any sign of a source at the same position in the H-Band ESM-data, possibly by reason that is is intrisically fainter in this band as well as the AO-system not being able to achieve a strehl value similar to the Ks-Band. You can clearly see the difference in resolution in the data before deconvolution and in the different FWHM of the PSF models.

Chapter 7

Summary and Perspective

The Quasar APM 08279+5255 is an individual object that has recieved a respectable amount of attention for numerous scientific studies since its discovery in 1998. It is an object of remarkable brightness at a considerably high redshift of z = 3.91, featuring an odd 3 component gravitational lensing system. However, the complete structure of this object has not yet been clarified. In order to verify existing models a lensing galaxy has to be found, which requires a deeper image at higher resolution than preivously achieved.

Therefore new data in the J,H and Ks-Band using the Large Binocular Observatories LUCI2 N30 camera has been aquired, that was reduced using flatfields, bad-pixel masks and a time and spatially adaptive background substraction. This background substraction method turned out to be the most effective one after comparing it to other approaches.

The data then was calibrated using photometric calibration points from the same observing run and magnitudes for the complete system have been measuren via aperture photometry. However, we quickly realised that the data, especially that in the Ks-Band was compromised by the PSF having a strikingly odd and assymmetrical shape. We conclude that intrinsic variations of the PSF as well as an erronoeus AO correction of some modes may have caused this shape. These problems were also present in other data-sets aquired during the same observation run, as reported by J.Heidt. This problem along with missing point sources in the FOV of the observations, rendered PSF photometry and PSF modelling problematic. Aperture photometry was used to compare our results to those of other authors and showed significant deviations, suggesting either an systematical error in the photometrical procedure or data reduction or variations of the quasars flux because of other reason such as gravitational microlensing or athmospherical conditions. We present a summary of all photometrical values obtained from different datasets by different techniques in a comprehensive table 6.2.

Additionally to the photometrical analysis we also conduct a number of attempts (despite the problems related to the PSF) on modelling the quasars components and aquiring residuals. These could have shown underlying unresolved objects, such as a lensing galaxy. Therefore we followed different

approaches using different PSF models, a simple Moffat profile and two synthetical PSFs created from the quasar components themselves. The resiudals showed artefacts due to unprecise PSF fitting and substraction, with the incapability of reconstruction the odd assymmetrical shape of the PSF as the major reason (see fig. 5.8 and 5.9 in CPT.5) of failure. Photometrical results were also obtained from the fits, but due to the problems the propability of them representing the real value of the object is expected to be minimal.

Nevertheless, when examining the FOV of the quasar in the N30 data, we found a possible candidate for a 4th component of the lensed system. Despite a large brightness contrast to the other objects, the systems geometry shows similarities to lensed QSO systems previously found. In order to confirm the membership of this object to the lensed system one has to both determine a color similar to those of the other components and a reasonable lensing model. Therefore we calculated the magnitude of this object in the H-Band and the required exposure time for a successful detection under the assumption of a membership to the system, aswell as a constraint of the lensing galaxy's position in section 4.4.

Furthermore, we used a different dataset of the same object taken by the LUCI2 N3.75 camera and ESM mode. We calibrated the data using 2MASS objects in the field and performed aperture photometry on the mostly unresolved lens system to compare values with those using the previous datasets. The photometrical measurements were those which compared best to the values of previous works and databases. The second objective was to search for the possible 4th component and therewith confirm it's existence, especially in the H-Band. It has been found in the Ks-Band using a Lucy-Richardson Deconvolution but showed evidence in the H-Band.

Perspective

One of the major objectives of this work was to lay the groundwork for a new model of the gravitational lensing system for which validation a lensing galaxy has to be found. To achieve the latter, a more precise and detailled modelling of the PSF is needed. One approach could be to use more advanced functionalities GALFIT offers, such as modelling of the azimuthal shape and combining multiple profiles (halo, moffat and diffraction limited theoretical PSF) using truncation functions.

With a PSF better representing the actual shape of the quasar components more possibilities of further analysis become available. Such would for example be using the software package DAOPHOT for PSF photometry, that should yield more accurate results than previously methods.

Another possibility would be to conduct further research on the 4th component candidate. This requires a deeper and better resolved data set in other filter bands in order to compare colors of

that object to those of the quasar components. Additionally to the constraint for the position of the lensing galaxy that has been made it might be recommendable to construct a more detailes lensing model based on the Ks-data already obtained, utilizing advanced modelling softwares such as GravLens.

Another research that is going to be done on this quasar is the search for a possible galaxy cluster in the FOV along the line of sight. That is one of the objectives to the ESM-data used for different purposes in this work. A discovery of the galaxy cluster in the FOV and the determination of it's approximate redshift would be a great hint for finding a lensing galaxy and one open parameter less for modelling the system.

Overall, one can conclude that this work didn't deplete the possibility of finding new impressive discoveries about this strange quasar...

Bibliography

[1] Peter Schneider: "Extragalactic Astronomy and Cosmology: An Introduction"

[2] Edward Harrison: "Cosmology: The Science of the Universe"

[3] Arnold Hanslmeier: "Einfuerung in Astronomie und Astrophysik", (2020)

[4] Bradley W. Carroll, Dale A. Ostlie: "An Introduction to Modern Astrophysics"

[5] J.Heidt, D.Thompson: "LUCI user manual", issue 1.98 First public release for comments

[6] J.Heidt: "Observing in the NIR -preparation, execution and data reduction", presentation at the 2017 NEON observing school, La Palma

[7] F.G.Saturni et. al.: "Restframe UV-to-optical spectroscopy of APM 08279 + 5255", A+A 617, A118 (2018), doi.org/10.1051/0004-6361/201832794

[8] Large Binocular Telescope Observatory: "Brochure LBTO 2017", available at www.lbto.org

[9] E.Egami et. al.: "APM 08279+5255 : Keck Near- and Mid-Infrared high-resoltuion imaging", ApJ 535 : 561574, 2000 June 1

[10] H.J.Witt:"Using Quadruple Lenses to probe the Structure of the Lensing Galaxy" , arXiv:astro-ph/9608197

[11] C.Peng: "Galfit user manual", distributed with every download of the galfit software package

[12] C.Peng et. al.: "Detailed Structural Decomposition of Galaxy Images ", AJ 124/266 (2002)

[13] M.Irwin et.al.:"APM 08279+5255: an ultraluminous BAL quasar at a redshift z=3.87", ApJ. 505 (1998) 529,arXiv:astro-ph/9806171[astro-ph.GA]

[14] J.P.McKean et.al.:"High-resolution imaging of the anomalous flux ratio gravitational lens system CLASS B2045+265: dark or luminous satellites?", R. Astron. Soc. 378, 109118 (2007), doi:10.1111/j.1365-2966.2007.11744.x

[15] R.M.Cutri et.al.:"2MASS All Sky Catalog of point sources", ADS 2003yCat.2246....0C, June 2013

[16] M.Blanton et.al.:"Sloan Digital Sky Survey IV: Mapping the Milky Way, Nearby Galaxies, and the Distant Universe", The Astronomical Journal, Volume 154, Number 1, pp. 28-62 (2017)

[17] D.E. Vanden Berk: "Composite quasar spectra from Sloan Digital Sky Survey",The Astronomical Journal, 122:549-564, 2001 August, iopscience.iop.org

[18] S.E.Persson: "A new system of faint near-infrared standart stars", The Astronomical Journal, 116 : 24752488, 1998 November

[19] S.Oya: "Spatially Resolved Near-Infrared Imaging of a Gravitationally Lensed Quasar, APM 08279+5255, with Adaptive Optics on the Subaru Telescope", PASJ: Publ. Astron. Soc. Japan 65, 9, 2013 February 25

[20] D.Riechers et.al.: "imaging molecular gas in a Z=3.9 quasar host galaxy at 0.3" resolution: a central, sub-kiloparsec scale star formation reservoir in APM 08279+5255, Astrophys.J.690:463-485,2009, also available at arXiv:0809.0754[astro-ph.GA]

[21] C.Feruglio et.al.:"On the discovery of fast molecular gas in the UFO/BAL quasar APM 08279+5255 at z=3.912", arXiv:1706.05527v2[astro-ph.GA]

[22] F.G.Saturni et.al.:"A multi-epoch spectroscopic study of the BAL quasar APM 08279+5255", arXiv:1512.03195v1[astro-ph.GA]

[23] D.C.Lis et.al.:"Discovery of water vapor in the high-redshift quasar APM 08279+5255 at Z=3.91", arXiv:1106.4784[astro-ph.CO]

[24] J.Heidt, W.Seifert et.al.:"LUCI1 & LUCI2 Comissioning Report", Issue 0.99 2803

Erklärung

Ich versichere, dass ich diese Arbeit selbstständig verfasst und keine anderen als die angegebenen Quellen und Hilfsmittel benutzt habe.

Heidelberg, den 6. Juli 2020,